Science of the Total Environment 918 (2024) 170686

Contents lists available at ScienceDirect

Science of the Total Environment

journal homepage: www.elsevier.com/locate/scitotenv

A novel post-1950 CE atmospheric ^{14}C record for the tropics using absolutely dated tree rings in the equatorial Amazon

Guaciara M. Santos[a,*], Daniela Granato-Souza[b,c,d], Santiago Ancapichún[e,f], Rose Oelkers[g], Heather A. Haines[h,i], Ricardo De Pol-Holz[e], Laia Andreu-Hayles[g,j,k], Quan Hua[l,m], Ana Carolina Barbosa[b]

[a] *Department of Earth System Science, University of California, Irvine, Irvine, CA, USA*
[b] *Department of Forest Sciences, Federal University of Lavras, Lavras, MG, Brazil*
[c] *Department of Geosciences, University of Arkansas, Fayetteville, AR, USA*
[d] *Department of Natural Resource and Environmental Sciences, Alabama A&M University, Huntsville, AL, USA*
[e] *Centro de Investigación GAIA Antártica (CIGA), Universidad de Magallanes, Punta Arenas, Chile*
[f] *Laboratorio de dendrocronología, Facultad de Ciencias Forestales y Recursos Naturales, Universidad Austral de Chile, Chile*
[g] *Lamont-Doherty Earth Observatory of Columbia University, Palisades, NY, USA*
[h] *Department of Earth and Environmental Science, The University of New South Wales, Australia*
[i] *Department of Geography, University of Nevada, Reno, USA*
[j] *Ecological and Forestry Applications Research Centre (CREAF), Bellaterra, Barcelona, Spain*
[k] *Catalan Institution for Research and Advanced Studies (ICREA), Barcelona, Spain*
[l] *Australian Nuclear Science and Technology Organisation, Lucas Heights, NSW, Australia*
[m] *School of Social Science, University of Queensland, St Lucia, QLD, Australia*

HIGHLIGHTS

- Nuclear bomb derived $^{14}CO_2$ has been detected in tree rings from Equatorial Amazon.
- A continuous atmospheric ^{14}C record from 1940 to 2016 was built with 175 measurements.
- Timing of tree-ring growth was verified by ^{14}C results of intra-annual wood slices.
- Longitudinal asymmetry has been found as well as terrestrial biosphere enrichment.
- Fossil $^{14}CO_2$ intrusion, mostly from the NH, has been detected from the 2000s onwards.

GRAPHICAL ABSTRACT

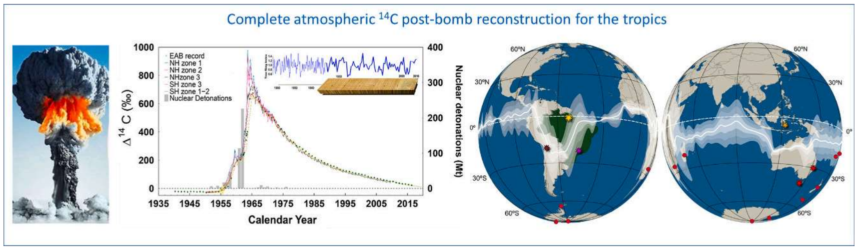

ARTICLE INFO

Editor: Elena Paoletti

Keywords:
Single tree-rings
Bomb peak
Atmospheric ^{14}C calibration

ABSTRACT

In this study, we present a comprehensive atmospheric radiocarbon (^{14}C) record spanning from 1940 to 2016, derived from 77 single tree rings of *Cedrela odorata* located in the Eastern Amazon Basin (EAB). This record, comprising 175 high-precision ^{14}C measurements obtained through accelerator mass spectrometry (AMS), offers a detailed chronology of post-1950 CE (Common Era) ^{14}C fluctuations in the Tropical Low-Pressure Belt (TLPB). To ensure accuracy and reliability, we included ^{14}C-AMS results from intra-annual successive cuts of the tree

---

[*] Corresponding author.
E-mail address: gdossant@uci.edu (G.M. Santos).

https://doi.org/10.1016/j.scitotenv.2024.170686
Received 24 November 2023; Received in revised form 19 January 2024; Accepted 2 February 2024

Atmospheric circulation
TLPB or Inter-Tropical Convergence Zone (ITCZ)

rings associated to the calendar years 1962 and 1963 and conducted interlaboratory comparisons. In addition, ^{14}C concentrations in 1962 and 1963 single-year cuts also allowed to verify tissue growth seasonality. The strategic location of the tree, just above the Amazon River and estuary areas, prevented the influence of local fossil-CO_2 emissions from mining and trade activities in the Central Amazon Basin on the ^{14}C record. Our findings reveal a notable increase in ^{14}C from land-respired CO_2 starting in the 1970s, a decade earlier than previously predicted, followed by a slight decrease after 2000, signaling a transition towards the fossil fuel era. This shift is likely attributed to changes in reservoir sources or global atmospheric dynamics. The EAB ^{14}C record, when compared with a shorter record from Muna Island, Indonesia, highlights regional differences and contributes to a more nuanced understanding of global ^{14}C variations at low latitudes. This study not only fills critical spatial gaps in existing ^{14}C compilations but also aids in refining the demarcation of ^{14}C variations over South America. The extended tree-ring ^{14}C record from the EAB is pivotal for reevaluating global patterns, particularly in the context of the current global carbon budget, and underscores the importance of tropical regions in understanding carbon-climate feedbacks.

1. Introduction

Before the industrial era, Earth's surface radiocarbon (^{14}C) levels were primarily influenced by the ^{14}C production rate in the upper atmosphere and its distribution among different reservoirs (Reimer et al., 2020). However, the past two centuries have seen marked shifts in atmospheric ^{14}C concentrations, largely due to the combustion of fossil fuels, virtually devoid of ^{14}C – known as the Suess effect (Suess, 1955) – and the introduction of bomb-derived ^{14}C from nuclear activities mainly in the 1950s to early 1960s (Levin and Hesshaimer, 2000). Grasping these human-induced influences on atmospheric ^{14}C and the Earth's subsequent responses is vital for understanding the carbon cycle, historical records, and anticipated climate changes (Kutschera, 2022).

To effectively capture and calibrate both past and current atmospheric ^{14}C fluctuations influenced by natural and human-made sources, we need comprehensive compilations of atmospheric ^{14}C levels. These should be drawn from dependable archives spanning various global locations (Hogg et al., 2020; Reimer et al., 2020; Hua et al., 2022). Current global compilations of post-1950 CE atmospheric ^{14}C are categorized into hemispheric and zonal datasets. These are further divided into summer for carbon-cycle research and zonal monthly data for precise ^{14}C dating of recent land samples (Hua et al., 2022). However, observational ^{14}C datasets near the equator, specifically within the Inter-Tropical Convergence Zone (ITCZ) over oceans or the Tropical Low-Pressure Belt (TLPB), remain sparse in detail and coverage (Reimer et al., 2020). For post-1950 CE ^{14}C calibrations, a tree-ring dataset from Muna Island, Indonesia (5°S, 122°E – dark-orange star in Fig. 1), spanning from 1950 to 1979, has been the primary reference for the entire December–January-February (DJF) TLPB up to the equator (Hua et al., 2022). It's worth noting that in this context, the DJF-TLPB aligns with the austral summer ITCZ as described by Hua et al. (2012).

In Graven et al. (2017), an atmospheric ^{14}C compilation spanning from 1950 to 2015 has been introduced aimed to represent the ^{14}C signatures characteristic of mid-year terrestrial materials located between 30°N and 30°S. While Hua et al. (2022) and Graven et al. (2017) compilations are valuable for general studies, their coarse resolution is insufficient for in-depth analysis of the relationship between atmospheric ^{14}C fluctuations, equatorial carbon-cycle processes, and tropical atmospheric circulation. Notably, the DJF-TLPB asymmetric zone, although confined over oceans, broadens considerably over continents (Fig. 1). The distinctive shifts of this zone and its migration from the Southern Hemisphere (SH) into the Northern Hemisphere (NH) and back can significantly alter rainfall in equatorial areas, leading to unexpected droughts or floods, as documented by Garreaud et al. (2009).

The migration of the TLPB across a vast region of South America (SA) significantly impacts the cross-equatorial $^{14}CO_2$ transport, which remains under-explored due to the absence of finely-tuned ^{14}C data, especially from pristine "clean air" locations (Santos et al., 2020). For calibrating equatorial pre-bomb ^{14}C ages, Hogg et al. (2020) proposed a streamlined approach that blends air-masses from both the Northern Hemisphere (e.g., IntCal20) and the Southern Hemisphere (e.g., SHCal20) in a 50:50 ratio, as detailed on http://intcal.org. Thus, enhancing our grasp on the ^{14}C isotopic distribution throughout SA will not only shed light on historical climate patterns and potential effects on early human settlements but also provide insights into the region's future climatic shifts.

Recently, Santos et al. (2015) and Ancapichún et al. (2021) developed two annually resolved ^{14}C records in SA, shedding light on the carbon-cycle's impact on atmospheric ^{14}C levels within DJF-TLPB influenced regions. Both records are positioned just north of the Tropic of Capricorn and on either side of the U-shape of the TLPB (Fig. 1). While both records are situated at nearly the same latitude, the Camanducaia, Brazil record (22°S, 46°W; 1927–1997) shows a ^{14}C enrichment from the 1970s onward when compared to the Irruputuncu record from the Altiplano in Chile (20°S, 68°W; 1950–2014). Air-parcel modeling by Ancapichún et al. (2021) suggests that positive ^{14}C biospheric fluxes from the Amazon Basin during the post-bomb period can influence adjacent areas near the TLPB boundary, elevating their atmospheric ^{14}C values. This observation aligns with findings from earlier carbon-cycle model evaluations (Randerson et al., 2002; Levin et al., 2010). Consequently, an increase in atmospheric ^{14}C levels is expected at the flux's source, specifically above the Amazon Basin.

In a study conducted at Porto Trombetas, Pará State, Brazil (1°S, 56°W; spanning 1938–2007), Santos et al. (2022) observed elevated atmospheric ^{14}C levels during the early 1970s. However, these levels declined significantly by the 1980s. By juxtaposing the ^{14}C data from Porto Trombetas with standalone tree-ring ^{14}C records from mid-latitude regions in SA, specifically Camanducaia (22°S, 46°W) and Irruputuncu (20°S, 68°W), Santos et al. (2022) inferred that the decline in atmospheric ^{14}C was influenced by local fossil fuel CO_2 emissions. These emissions were linked to the expansion of mining activities and river trade networks in Pará State. Notably, the study likely underestimated the fossil fuel CO_2 contributions, e.g., the maximum excess was estimated as 6.3 ± 0.8 ppm when nonideal baselines were used as reference (Santos et al., 2022). While the latter study provided valuable insights, it highlighted the potential for further refinement in estimating fossil fuel CO_2 contributions in the central Amazon Basin as well as the importance of incorporating comprehensive equatorial atmospheric ^{14}C records from the region's untouched areas. This perspective reinforces the need for additional high-quality atmospheric ^{14}C records, enabling researchers to delve deeper into the primary carbon sources that shape atmospheric ^{14}C dynamics within the TLPB.

Building upon prior research, our study presents a unique and comprehensive tree-ring ^{14}C record from the Eastern Amazon Basin (EAB), Brazil (1°S, 53°W – highlighted in Fig. 1). This ^{14}C record, derived from a dendrochronologically dated *Cedrela odorata* tree (Granato-Souza et al., 2019, 2020) in a notably pristine environment, offers fresh insights into terrestrial biosphere reservoir effects and atmospheric dynamics over the Amazon Basin. Our findings not only contribute to the broader understanding of ^{14}C distributions at low latitudes but also shed light on the intricate interplay between carbon-cycle dynamics and atmospheric circulation above the Amazon.

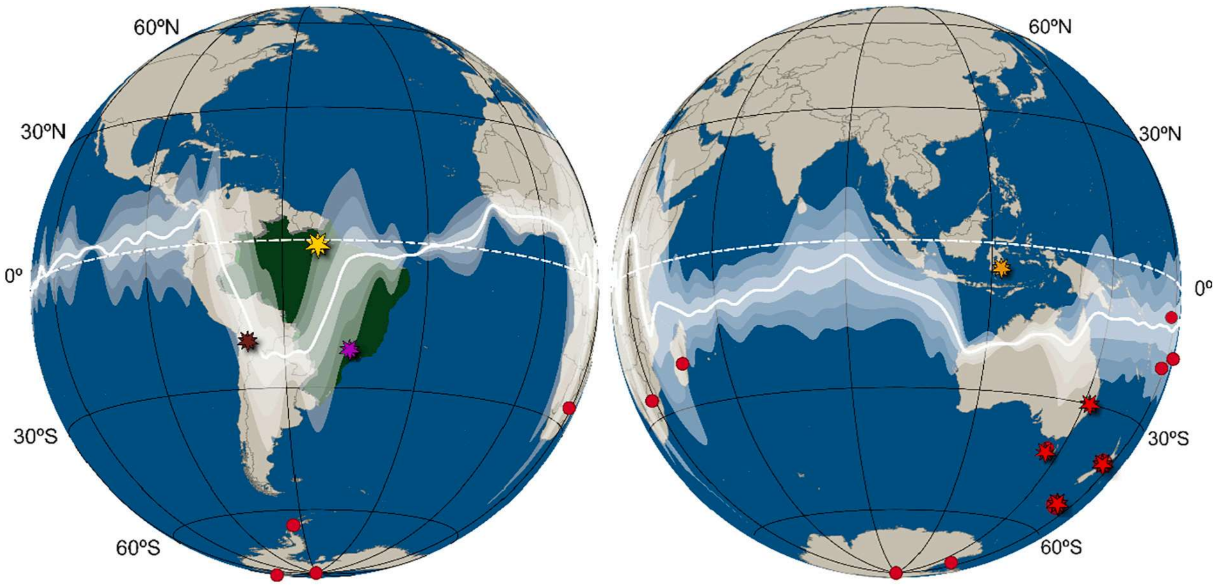

Fig. 1. Diagrammatic representation of the sites and datasets included in the zonal divisions for the Southern Hemisphere (SH) compilation of Hua et al. (2022). The white line represents the average (±1σ, ±2σ, and ±3σ; white ribbon) latitudinal positions of the Tropical Low-Pressure Belt (TLPB) over land and oceans, occasionally referred as the intertropical convergence zone (ITCZ) in some studies. It was produced by taking the 1948–2020 averaged austral summer (DJF) minimum sea level pressure between 10° N and 35° S in the NCAR/NCEP reanalysis. **Current datasets from atmospheric stations and tree ring sites are:**
SH zone 1–2 [Antarctica to DJF-TLPB]: Scott Base, Antarctica (78°S, 167°E; 1961-1972 & 1973–1976; Manning et al., 1990), Palmer Station (65°S, 64°W; 2005–2007; Graven et al., 2012), South Pole (90°S, 25°W; 1984-1992 & 1999-2007; Meijer et al., 2006; Graven et al., 2012); Campbell Island, New Zealand (*53°S, 169°E; 1953–1972* & 53°S, 169°E; 1970-1971 & 1973-2011; Manning et al., 1990; Turney et al., 2018); Tasmania, Australia (41°S, 145°E; 1953-1976; Hua et al., 2000); Wellington, New Zealand (*33–41°S, 174.8°E; 1951–1972* & 41°S, 175°E; 1954–2019; Turnbull et al., 2017); Cape Grim, Australia (40°S, 144°E; 1993–2008; Levin et al., 1996, 1999, 2011); Armidale, Australia (30°S, 152°E; 1953–1977; Hua et al., 2003); Pretoria, South Africa (25°S, 28°E; 1950-1994; Vogel and Marais, 1971); Fianarantsoa, Madagascar (21°S, 47°E; 1964–1978; Nydal and Lövseth, 1996); Suva, Fiji (18°S, 178°E; 1958-1975; Manning et al., 1990); Cape Matatula, American Samoa (14°S, 171°W; 2001–2007; Graven et al., 2012); Funatufi, Tuvalu (8.5°S, 179.2°E; 1966–1972; Manning et al., 1990). Tree-ring records are represented by red stars and atmospheric stations by red circles. For those sites that show both types of records the calendar years associated with the tree-ring periods are italicized.
Recent tree-ring ^{14}C records added to SH zone 1-2: Camanducaia, Minas Gerais, Brazil (22°S, 46°W; 1927–1997) [Santos et al., 2015] – represent by purple star; Irruputuncu, Altiplano (20°S, 68°W; 1950-2014) [Ancapichún et al., 2021] - represented by brown star.
SH zone 3 [DJF-TLPB to equatorial line]: Muna Island, Indonesia (5°S, 122°E; 1950–1979) [Hua et al., 2012] – represented by dark-orange star. Note that due to lack of ^{14}C records from 1979 onward, SH zone 3 compilation of Hua et al. (2022) makes use of the same datasets in SH zone 1–2 compilation from 1979 to 2019.
New record to be added to SH zone 3: Eastern Amazon Basin (EAB), Brazil (1°S, 53°W; 1940–2016) [This study] - represented by bright-yellow star.

2. Materials and methods

2.1. Eastern Amazon Basin tree species site and dendrochronological characteristics

Cedrela species are well-documented in SA dendrochronology for their consistent formation of annual rings in locations with a unimodal rainfall pattern (Baker et al., 2017). Granato-Souza et al. (2019) constructed a 231-year chronology for *C. odorata*, covering the period from 1786 to 2016 (Fig. 2), based on the Paru State Forest samples (0.977°S, 53.326°W; 200 m a.s.l.). This chronology, derived from the most synchronously growing trees (27 trees and 56 radii), has been shown to align positively with regional rainfall data. Moreover, this chronology is significantly influenced by the overarching climate dynamics of the EAB (Granato-Souza et al., 2019, 2020). Situated within the tropical rain belt (Fig. 1), this chronology's location is pivotal. The region's biomass is influenced by the north-south movements of the TLPB and the effects of El Niño Southern Oscillation (ENSO) (Garreaud et al., 2009; Stahle et al., 2020), highlighting its importance for future studies.

The climate of Paru State Forest features high annual temperatures, averaging 27.2 °C, and seasonal rainfall, with an annual average of 1970 mm. The wet season runs from December (previous year) to July (current year), followed by a shorter dry season from August to November (current year) (Granato-Souza et al., 2019) (Fig. 2). Despite its proximity to the 'insolation equator' (Borchert et al., 2005, 2015), the growth of *C. odorata* in the EAB is primarily influenced by rainfall patterns rather than daily insolation (Granato-Souza et al., 2019, 2020). These authors used data from the Global Precipitation Climatology Centre (GPCC) to find that the growing season for *Cedrela* in this area appears to be rather short, occurring between February and July (Fig. 2). This timing is crucial for understanding when carbon dioxide, and by extension $^{14}CO_2$, is absorbed and stored in *C. odorata* at this site.

2.2. Sample selection and processing

The construction of the *C. odorata* long homogeneous ring-width chronology from the Paru State Forest (0.977°S, 53.326°W) has been extensively detailed in prior works (Granato-Souza et al., 2019, 2020). For this study, the *C. odorata* specimen was sourced from the established 231-year tree-ring chronology (Fig. 2), which was developed by overlapping the ring widths from 27 trees, encompassing 56 radii. A distinct wood segment, labeled P45, approximately 5 cm thick, was extracted from a cross-section that exhibited exceptionally clear tree rings with well-defined boundaries at the Universidade Federal de Lavras (UFLA), Brazil. Seventy-seven annual tree rings spanning the period 1940 to 2016 were individually sampled for high-precision ^{14}C and stable isotope (δ^{13}C) analysis. The majority of these rings were wider than 2 mm, ensuring that samples could be distinctly separated at both the terminal and initial parenchyma bands, without incorporating material from adjacent rings. The height dimensions of the rings also facilitated cross-cutting for comprehensive growing-season replication analysis, as well as for obtaining intra-annual wood slices from the 1962 and 1963 calendar years. The subsequent sections provide detailed procedures on the preparation of wood samples and subsamples for isotopic analysis, as illustrated in Fig. 3.

Samples, labeled by their respective calendar years, were sent to the Keck Carbon Cycle AMS (KCCAMS) facility at the University of California, Irvine (UCI). Here, they underwent various processes such as microscope inspection to verify the full growth season (Fig. S1 in the supplementary material), weight data collection, and sub-sampling for duplication analysis (Fig. 3A and C). The whole-wood samples spanning from 1940 to 2016 were then forwarded to the Lamont-Doherty Earth Observatory (LDEO) for cellulose extraction via batch processing. After this step, they were returned to KCCAMS/UCI for ^{14}C analysis. A secondary set of samples consisting of intra-annual wood samples from the years 1962 and 1963, along with the complete rings from the same years, were meticulously prepared at UFLA. These samples were specifically sent to KCCAMS/UCI to undergo chemical treatments and subsequent ^{14}C determinations at this facility (Fig. 3B). Additionally, a specific subset of 10 whole-wood samples spanning the years 1990 to 2000 was dispatched to the Australian Nuclear Science and Technology Organisation (ANSTO) for cross-laboratory validation (Fig. 3C). Since the ring of 1999 CE contained insufficient material for accurate duplication of its growing season, it was replaced by 2000 CE's ring to complete the set. Note that this cross-laboratory validation involved both chemical extraction and ^{14}C analysis. In summary, tree-ring cellulose extracts were processed in all three laboratories (LDEO, KCCAMS/UCI and ANSTO), but the graphite sample processing and radiocarbon measurements were conducted in two ^{14}C-AMS facilities (KCCAMS/UCI and ANSTO). For further details see Fig. S2 in the supplementary material.

To guarantee the measurement of only the structural carbon from the post-bomb ^{14}C tree rings, and to obtain the correct ^{14}C signatures associated with the carbon assimilated in the corresponding growth year, α-cellulose extraction procedures were adopted across all involved laboratories: KCCAMS/UCI, LDEO, and ANSTO. This approach is crucial to avoid any interference from carbohydrates from later calendar years, ensuring the purity of the samples for ^{14}C analysis (Santos et al., 2020, 2023). Refer to Figs. S1 and S2 for details on sample handling evaluations and subsampling, as well as the aforementioned laboratories' chemical protocols and main devices used.

To assess the background level and ensure quality control of the chemical procedures and apparatus, ^{14}C-free AVR wood, post-bomb FIRI-J barley mash, and FIRI-H sub-fossil wood were measured at KCCAMS/UCI and processed together with α-cellulose samples extracted at LDEO and KCCAMS/UCI (Scott et al., 2003a, 2003b). The ANSTO facility utilized its own reference materials, including FIRI-J and TIRI-J wood, as well as IAEA-C3 cellulose (Scott et al., 2003a, 2003b; Rozanski et al., 1992), and employed sub-fossil Kauri wood and spectroscopic grade powdered ^{14}C-free graphite from Union Carbide Corporation as blank materials.

2.3. Isotopic analysis

2.3.1. Corroboration of temporal growth pattern

To accurately align the dendrochronological calendar years of the complete growing season with the actual time of tissue formation, and subsequently with the atmospheric ^{14}C dioxide fixation during the wet season (Fan et al., 1990), we focused on two consecutive calendar years, 1962 and 1963, which exhibited significantly different atmospheric

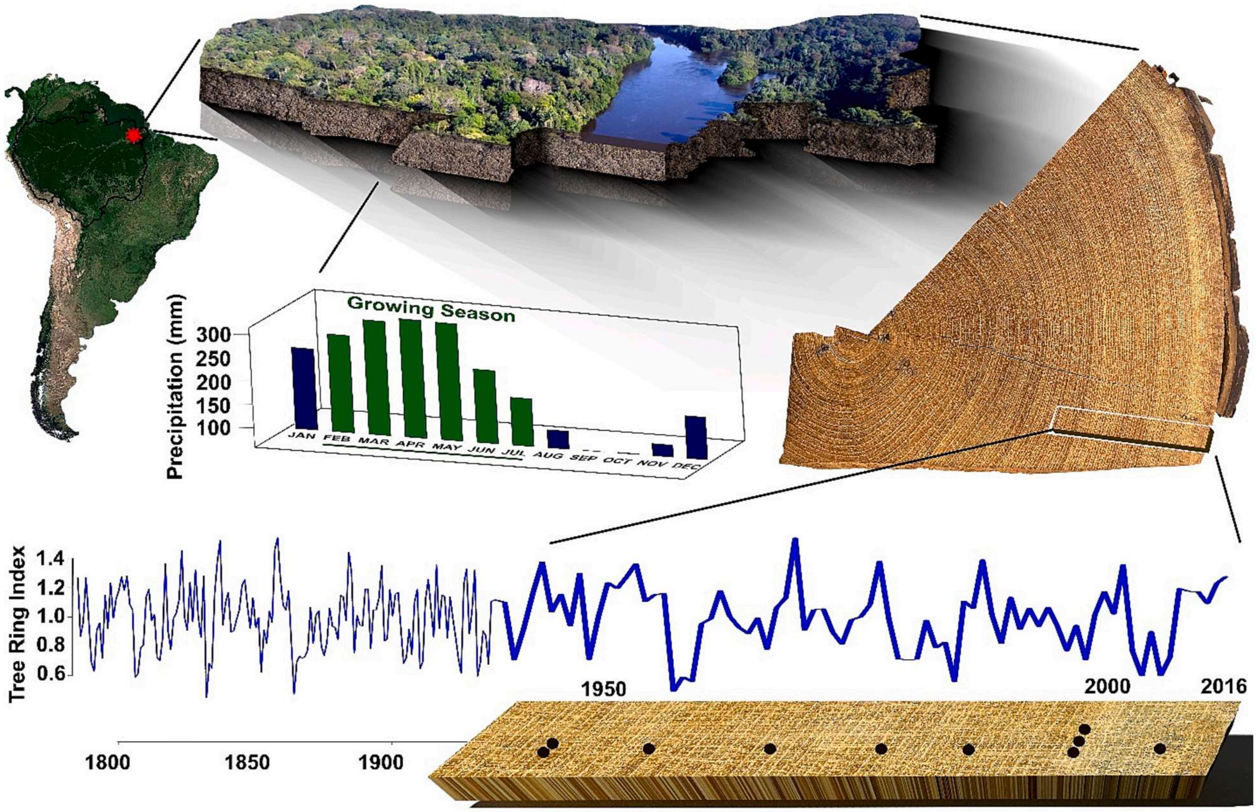

Fig. 2. Sampling location at the Eastern Amazon Basin, Brazil (0.977°S, 53.326°W; 200 m asl - red star), followed by the Paru State Forest representation. Monthly average precipitation (navy/green bars) was calculated from climate gridded data extracted from CRU TS4.00, (5°N–5°S, 60°–53°W). Months that are specifically represented in green bars depict the growth period of *C. odorata* based on climate-growth relationship analysis (Granato-Souza et al., 2020). Cross-section view and *C. odorata* ring-width chronology (1786–2016), portraying the wood-segment used in this study (1940–2016), are also illustrated as a simplified schematic representation. The wood-segment and associated tree-ring curve section from 1940 to 2016 have been strongly magnified and therefore, do not accurately represent their actual scales. Black circles demark the decadal horizons of 1950 (two black circles), 2000 (three black circles), and one dot for the others.

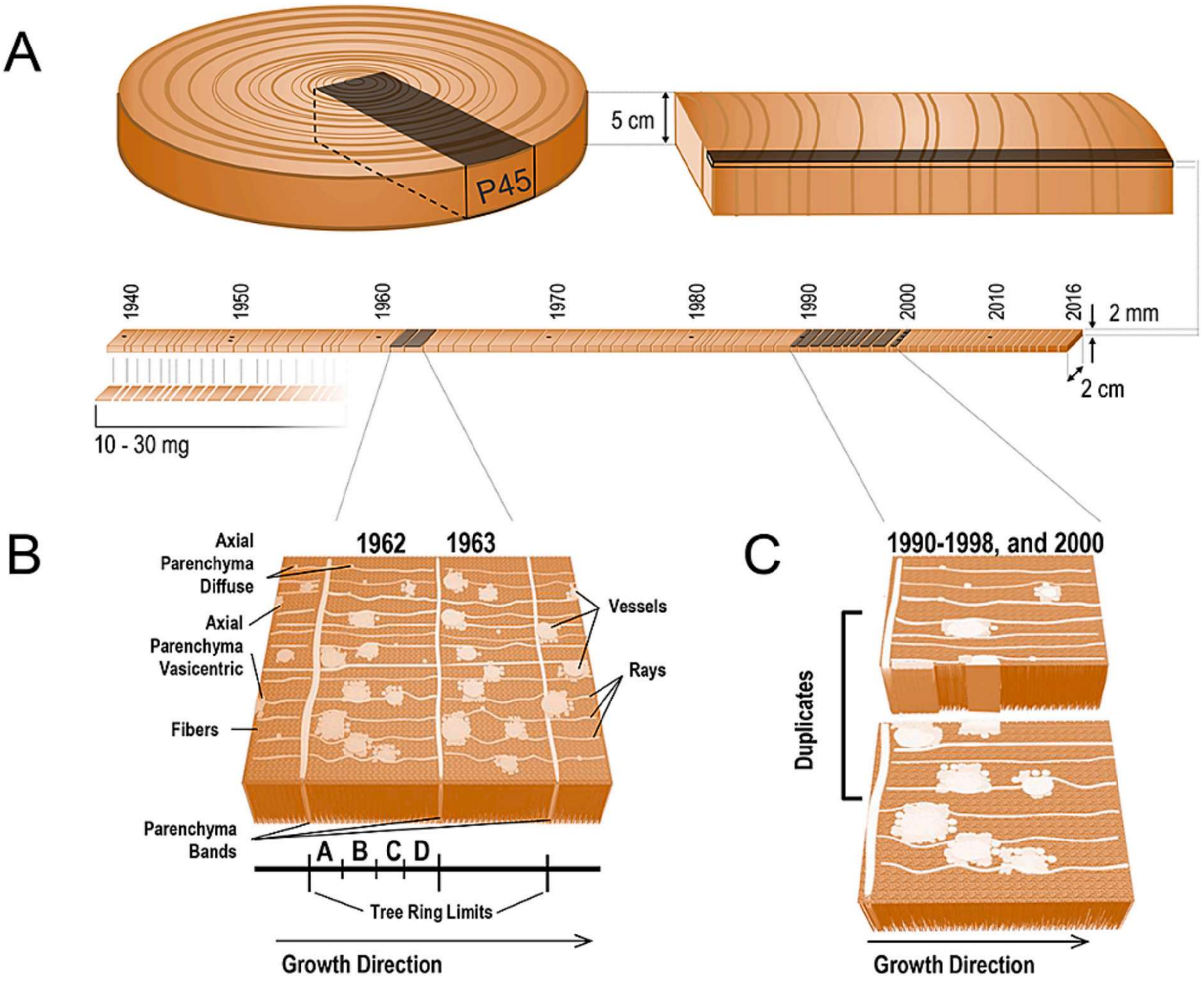

Fig. 3. Schematic drawing of the *C. odorata* cross-section, wood segment, and thin radial specimen cut that helped with preparation of subsamples (A). Intra-annual slices of the tree rings from 1962 and 1963 calendar years. Samples were dissected with a scalpel (B). Schematic drawing of tree-ring duplicates for ^{14}C-AMS interlaboratory comparison (C). Tree-ring illustrations show the different features of parenchyma tissue, fibers, and vessels. For details on subsampling rationality, see text.

Δ^{14}C signals. The wood from these years was divided into four equal parts along the tangential plane by the UFLA dendrochronology team, as illustrated in Fig. 3B. For time scale of the 1962 and 1963 slices, we assumed a constant radial growth from February to July. Grootes et al. (1989) and Svarva et al. (2019) demonstrated that site location, climate, species, and tree age all combined would give similar growth curves with a very small margin of error that would not overtly influence temporal assignment of sub-annual Δ^{14}C signals. Thus, we estimated the approximate stem growth span from February 01 to July 30, based on the climate diagram of Granato-Souza et al. (2019, 2020), using this constant growth assumption to delineate the timing associated to each slice as shown in Fig. S3 in the supplementary material.

Following the α-cellulose extraction process at the KCCAMS facility, which is thoroughly described in Santos et al. (2023) and summarized in Fig. S2A, the four consecutive cuts were subjected to isotopic analysis to determine their intra-annual ^{14}C signatures, as detailed in the subsequent Section 2.3.2 and Fig. S3. The radiocarbon results were then compared with the ^{14}C values obtained from the full growing season analogs, which were chemically extracted at both the LDEO and KCCAMS/UCI.

2.3.2. Radiocarbon time-series

To establish a comprehensive ^{14}C record of tree rings from 1940 to 2016, involving 77 individual rings, KCCAMS/UCI shipped single whole-rings to LDEO to convert them to α-cellulose utilizing 150-funnel device submerged in a controlled-heated water bath (Andreu-Hayles et al., 2019) and chemical method previously optimized for ^{14}C analysis and validated by Santos et al. (2020). These cellulose fibers, along with those obtained from the intra-ring wood cuts mentioned in Section 2.3.1, were subsequently transformed into filamentous graphite following well-established protocols at KCCAMS facility (Santos and Xu, 2017) to latter undergo high-precision ^{14}C-AMS measurements. A total of 155 radiocarbon measurements were conducted using a modified NEC 0.5MV 1.5SDH-1 spectrometer at KCCAMS/UCI, equipped with online δ^{13}C-AMS capabilities to enhance the isotopic-fractionation correction of the ^{14}C data (Beverly et al., 2010). This ensured a precision of 2 ‰ or better for all measurements taken across 8 total ^{14}C-AMS wheels, with 6–7 measurements of Oxalic acid I (OX-I or NIST HOxI SRM 4990B) used as the primary standard.

The results of the tree-ring ^{14}C analysis are presented as decay-corrected Δ^{14}C values, expressed in parts per thousand (‰), which can be calculated according to

$$\Delta^{14}\mathrm{C} = \left\{\mathrm{F}^{14}\mathrm{C}\cdot exp[-\lambda(T_i - 1950)] - 1\right\}\cdot 1000 \quad (1)$$

where F^{14}C is the normalized ^{14}C concentration to a certified standard, such as OX-I; λ is the decay constant of 8267y^{-1} for ^{14}C; and T_i is the calendar year of wood tissue formation.

This method of expression follows the protocols established by

Stuiver and Polach (1977), and further detailed by Santos et al. (2007). To ensure the reliability of our results, we conducted several duplicate and triplicate analyses, using different aliquots of α-cellulose extracts. In some cases, independent wood cuts were also utilized to further validate our findings. For further details on LDEO chemical protocol and ^{14}C sample processing see Fig. S2B in the supplementary material.

2.3.3. Radiocarbon inter-laboratorial validation

Ten wood subsamples from the full growing seasons spanning 1990–1998 and 2000 CE were sent to ANSTO for ^{14}C-AMS validation and inter-laboratorial analysis (Fig. 3C). The α-cellulose extraction followed a modified method from Hua et al. (2004), and the samples were subsequently converted to graphite targets as per Hua et al. (2001). For further details on ANSTO chemical protocol and ^{14}C sample processing see Fig. S2C in the supplementary material.

A portion of the graphite was analyzed using EA/IRMS to determine its δ^{13}C value, aiding in isotopic fractionation correction of the ^{14}C data. Radiocarbon measurements were conducted using the 1-MV NEC VEGA accelerator at ANSTO, achieving a precision better than 2.5 ‰ (Fink et al., 2004). All samples were processed in duplicate, with OX-I serving as the primary standard for ^{14}C determinations. The tree-ring ^{14}C results were converted to decay-corrected Δ^{14}C ‰ using Eq. (1), and then compared with the ^{14}C signatures from the corresponding calendar years measured at KCCAMS/UCI facility.

2.3.4. Suess effect on the stable carbon isotope

We utilized the remaining α-cellulose fibers from our comprehensive tree-ring record to derive empirical δ^{13}C Suess effect values for the EAB site. The Suess effect, predominantly caused by the release of isotopically lighter carbon from fossil-fuel combustion, results in a reduction of atmospheric δ^{13}C values (Keeling et al., 2017). Consequently, a time series of δ^{13}C values can serve as an indicator of fossil-fuel impact at specific locations (Turney et al., 2018).

For each tree-ring sample, we placed approximately 0.7 mg of α-cellulose into 5 × 8 mm tin foil capsules. We then determined the stable carbon isotope ratios (i.e., δ^{13}C) using a continuous-flow FISONS NA 1500 NC Elemental Analyzer connected to a Delta-Plus CF-Isotope Ratio Mass Spectrometer at the KCCAMS/UCI facility. The precision of our elemental analyzer and mass spectrometer setup for δ^{13}C is typically around 0.1 ‰, as verified by repeated measurements of both in-house standards and internationally recognized reference materials, such as USGS-24, IAEA-600, and Atropine ($C_{17}H_{23}NO_3$). Where feasible, duplicate samples were analyzed to ensure consistency, and the precision of our measurements was in line with that of the reference materials used.

2.4. HYSPLIT atmospheric transport and dispersion model

The Hybrid Single-Particle Lagrangian Integrated Trajectory (HYSPLIT) model (Stein et al., 2015), was utilized to generate geographic provenance (GP) maps for tracing the source and destination of air parcels transporting $^{14}CO_2$ to our sites of interest. HYSPLIT version 4 is an advanced system for calculating air-parcel trajectories, including complex transport, dispersion, chemical transformation, and deposition simulations. Backward trajectories, which provide longitudinal, latitudinal, and altitudinal data points tracing an air parcel's path back in time, were generated based on the default altitude of the ground level of the input-data for each region, following the approach of Draxler and Taylor (1982). Input data for the HYSPLIT model were sourced from satellite and in-situ atmospheric observations, as part of the NCEP/NCAR reanalysis project (Kalnay et al., 1996). Building on the findings of Ancapichún et al. (2021, 2022), which suggested that modeling an air parcel's backward trajectory for 1 h per day could effectively approximate a full day's trajectory. We adopted this streamlined approach to assess the contributions of air parcels from each hemisphere to the study sites, using a single midday air parcel backward trajectory per day for our analysis.

In this study, we focused on air parcels reaching two specific locations: EAB (1°S, 53°W; with 130 m as default altitude from ground level) and Muna Island (5°S, 122°E; with 51 m as default altitude from ground level). The choice of Muna Island for comparison with our site was twofold: firstly, the tree-ring ^{14}C data from Muna Island, spanning 1950–1979, has been pivotal in developing the atmospheric ^{14}C intra-hemispheric SH zone 3 model (DJF-TLPB; see Fig. 1; Hua et al., 2022), and secondly, early January has been identified as the average time for tissue growth at this site. The growth of *Tectona grandis* wood on Muna Island, located in South Sulawesi (Hua et al., 2012), was determined by the rainy season in the Indonesian archipelago, which typically extends from November to April (Aldrian and Susanto, 2003). It is important to note that the growing season months of *T. grandis* wood on Muna Island slightly differs from that of *C. odorata* at the EAB site, which very likely experiences growth from February to July (refer to Fig. 2).

For the case study, we analyzed air parcel transportation changes occurring 5 to 25 days into the past, in 5-day increments (at −120, −240, −360, −480, and −600 h), spanning from 1949 to 2016. This analysis aimed to identify potential sources of air parcels carrying $^{14}CO_2$ that reached the EAB and Muna Island sites and could be assimilated into wood tissue during growth. The study included air parcels from both north and south of the TLPB, accounting for contributions from the NH and/or SH over the period from 1949 to 2016. Additionally, we examined air parcel transportation changes occurring 1 to 5 days into the past (−24, −48, −72, −96, and −120 h) specifically for the EAB site. This focused analysis aimed to elucidate how air masses approach this location north of the Amazon River's mouth.

While the growth periods for trees at EAB (February to July) and Muna Island (November to April) are not synchronized (occurring in different months of the year), the duration of tissue growth is similar, averaging the same number of days for completion. Consequently, we modeled 181 air parcels per year for each location, representing one backward trajectory per day. For each time window (−120, −240, −360, −480, and −600 h), a total of 12,308 backward trajectories (i.e., 181 trajectories × 68 years) were analyzed for each site. The atmospheric circulation boundary between the NH and SH was defined by the averaged position of the TLPB calculated for each month and year studied. To calculate the percentage of air parcel GPs originating from the NH and SH, we averaged the annual series by dividing them by 1.81 (181/100). The GP maps, along with the total averaged percentage contributions for each time window, are presented in Section 3.2, followed by discussions.

3. Results and discussion

3.1. Reliability tests for the EAB ^{14}C record

To ensure the accuracy of atmospheric post-1950 CE ^{14}C data, it is crucial to use only tree-ring records without any flaws. In this regard, the robustness of the *C. odorata* tree-ring width chronology was initially verified through high-precision ^{14}C-AMS analysis of selected calendar years, with the findings reported in Santos et al. (2020). Here, we present a complete sequence spanning from 1940 to 2016, comprising 175 ^{14}C measurements. The individual ^{14}C data obtained from this study will be made available in a dataset repository for future research and analysis (refer to the Data Availability Statement for more details).

Fig. 4A illustrates the mean values of the complete EAB ^{14}C record alongside the SH ^{14}C compilations as described in Hua et al. (2022). Even though these compilation curves were derived from discontinuous historical datasets (as shown in Fig. 1), and the SH zone 3 data from 1979 onwards was derived from SH zones 1–2 datasets, the EAB ^{14}C record aligns well with them. For radiocarbon results with more than one measurement, which accounts for over 80 % of the samples in this dataset, uncertainties are calculated based on error-weighted averages. The remaining ^{14}C results, specifically a few calendar years before 1950, 1987, and the 1962/1963 calendar year slices (4 samples each – as depicted in Fig. 4B), display the conventional ±1 σ uncertainty after undergoing propagated corrections such as normalization, isotopic fractionation, and background corrections. In Fig. 4A, these uncertainties are obscured by the symbols used in the plots. The pooled standard deviation, derived from 69 replicated measurements including those from independent chemical extraction procedures and ^{14}C-AMS facilities, yielded a precision of 0.13 %, confirming that the data overall exhibits very little deviation.

To validate the alignment of the EAB ^{14}C record with compiled mean values of atmospheric post-bomb ^{14}C, and to affirm its significance for equatorial SH latitudes, additional data reliability tests were conducted.

1) To verify that the EAB ^{14}C dataset from 1940 to 1955 (pre-bomb period) is free from anomalies due to sapwood-heartwood mobility (the "Cain effect" as described by Cain and Suess (1976)), we conducted a thorough evaluation. The Cain effect was initially believed to be more pronounced around the 1930s, as per Tans et al. (1978), but can appear as late as 1962 or 1963 if improper chemical extractions are used (Westbrook et al., 2006). Our analysis, particularly for the early portion of the dataset shown in Fig. 4A (the period 1940 to 1955), confirms the absence of interference from secondary metabolites due to sapwood-heartwood translocation. This ensures that the EAB ^{14}C record accurately reflects atmospheric ^{14}C levels.
2) We assessed the age-dependency of radial growth tissue for our ^{14}C record to align it with the dendrochronological calendar years and the climate-growth relationship detailed in Granato-Souza et al. (2020). This involved examining the progressive wood formation for the years 1962 and 1963, as shown in Fig. 3B. The results, displayed in Fig. 4A and highlighted in Fig. 4B, indicate that the best data-fitting solution for calendar growth increments versus ^{14}C signatures was achieved when ^{14}C results were evenly distributed over the six months from February to July. Regardless of the uncertainties associated with the assignment of a certain growing period to each wood slice measured, sub-annual increment ^{14}C results fit well with the whole-ring counterpart ^{14}C result of each calendar year tested (Fig. 4B). Specifically, the optimal fit for single ^{14}C data points from whole rings occurred when the ^{14}C results for either 1962 or 1963 whole rings aligned adjacent to the second succeeding cut of the tree-ring short-segment on the graph (Fig. 4B, around early April). To an extent, this suggests slightly rapid growth during established precipitation and a slowdown in growth towards the end of the wet season (Fig. 1). Consequently, we applied a revised decimal time fraction correction of 0.34 years to the dendrochronological dates for the whole-ring 1962 and 1963, as well as to all other dendrochronological calendar years associated with the EAB ^{14}C record shown in Fig. 4A. This sub-annual correction, which more accurately defines the annual growth timing for *C. odorata* at this location, aligns with the average whole growth tissue period defined by Granato-Souza et al. (2020). However, this new time fraction correction of 0.34 years differs by 0.06 years than that used in Santos et al. (2020). Although small, this adjustment is significant for a more precise indication of the ^{14}C level determined for each calendar year.
3) For high-resolution ^{14}C analysis, we verified the reproducibility and accuracy of ^{14}C-AMS measurements through an inter-laboratory test between KCCAMS/UCI and ANSTO. Ten replicate tree-ring samples were analyzed (Fig. 3C). Both facilities measured graphite targets from different α-cellulose extracts, employing distinct spectrometer types and lab techniques for isotopic data and corrections. KCCAMS/UCI produced single results for each tree-ring sample with an average uncertainty of <0.18 %, while ANSTO provided duplicates for the same calendar years, with an average error of 0.23 %. A pooled standard deviation based on these 10 paired measurements yielded an outstanding precision of 0.17 % (Fig. 4C).
4) Finally, the EAB ^{14}C record, presented as $\Delta\Delta^{14}$C (Fig. 4D), was aligned with the SH zone 3 baseline to highlight significant data differences. Detailed interpretations of the Δ^{14}C differences shown in Fig. 4D are provided in Section 3.3, supported by the air flow maps in Section 3.2.

3.2. Cross-equatorial air flow maps

Due to the TLPB's reach from the equator into both hemispheres, equatorial sites are likely influenced by air parcels from both the NH and SH, particularly within the 30°N to 30°S range, as per general atmospheric mixing patterns (https://www.noaa.gov/jetstream/global/jet-stream). In the austral summer, the NH's circulation cells near the equator are at their peak, enabling faster horizontal transport of air masses (Wu et al., 2018). However, slight seasonal and interhemispheric asymmetries are expected (Yan et al., 2021). Consequently, the minor but noticeable differences between the EAB ^{14}C record and the SH zone 3 compilation (Hua et al., 2022), as shown in Fig. 4D, require further exploration.

To understand the interhemispheric variances in ^{14}C at the EAB (1°S, 53°W; 200 m a.s.l. - this study) and Muna Island (5°S, 122°E; 0–150 m a.s.l.), i.e., sites at similar latitudes but diametrically opposed from each other in terms of longitudes, we utilized the HYSPLIT model (Stein et al., 2015) in conjunction with NCEP/NCAR reanalysis data (Kalnay et al., 1996). This approach was chosen to facilitate discussions on ^{14}C differences at these longitudinally opposite sites. Our analysis included backward trajectory totals of 12,308 (Section 2.4), aligned with the specific tissue growth periods of each tree species/site. Notably, the *C. odorata* at EAB and *T. grandis* at Muna Island have different growth periods, from February to July and November to April, respectively. These specific growth periods were factored into the GP modeling. The resulting TLPB atmospheric circulation boundary between the NH and SH hemispheres is visually represented in the accompanying figures.

Our results are presented in various formats: (1) We analyzed GP back trajectories reaching the EAB and Muna Island sites for five specific hours into the past (−120, −240, −360, −480, and −600 h) over the period from 1949 to 2016, as illustrated in Fig. 5A. The total averaged percentages of these trajectories are detailed in Table 1. (2) We also examined GP back trajectories reaching the EAB site for the following hours into the past: −24, −48, −72, −96, and −120, depicted in Fig. 5B. (3) To provide a time-series analysis of air parcel contributions (in %) from both the NH and SH arriving at the EAB and Muna Island sites from 1949 to 2016 for a specific time-window, we calculated the percentage of air parcels originating from the NH and SH for −600 h, as shown in Fig. 6. Additionally, Table S1 in the supplementary material presents the annual averaged percentages and their associated standard deviations, correlating with the data in Fig. 6.

The composite means of above sea level pressure indicate significant differences in the orientation of air masses reaching the Amazon Basin and/or crossing the Indonesian archipelago during the five specific hours into the past (Fig. 5A). Air masses reaching the EAB seem to primarily originate from the Atlantic Ocean's extratropical region, the northwestern African coast, western Europe, and possibly the eastern side of the US, though the eastern southern African coast cannot be entirely discounted (Fig. 5A – left panels). Backward trajectories over the Indonesian archipelago suggest that air masses were transported to Muna Island mainly from North China and the South China Sea, as well as the North Pacific Ocean. Subsequently, air masses concentrated within a relatively small grid over the Indonesian archipelago (e.g., 10°S–10°N, 100–130°E), likely due to the Asian monsoonal circulation (Fig. 5A – right panels), which produces seasonal reversing winds and precipitation patterns as noted by others (Hua et al., 2012 and references therein). Contributions of air parcels to Muna Island from the SH, particularly from over Australia, are also evident.

In Fig. 5, the TLPB atmospheric circulation boundary between the NH and SH (solid white line in Fig. 5A and dashed gray line in Fig. 5B) is arched, but less pronounced compared to the DJF-TLPB shown in Fig. 1 or as depicted in Hua et al. (2022). The TLPB shifts following solar radiation, so its average position from February to July (EAB) or

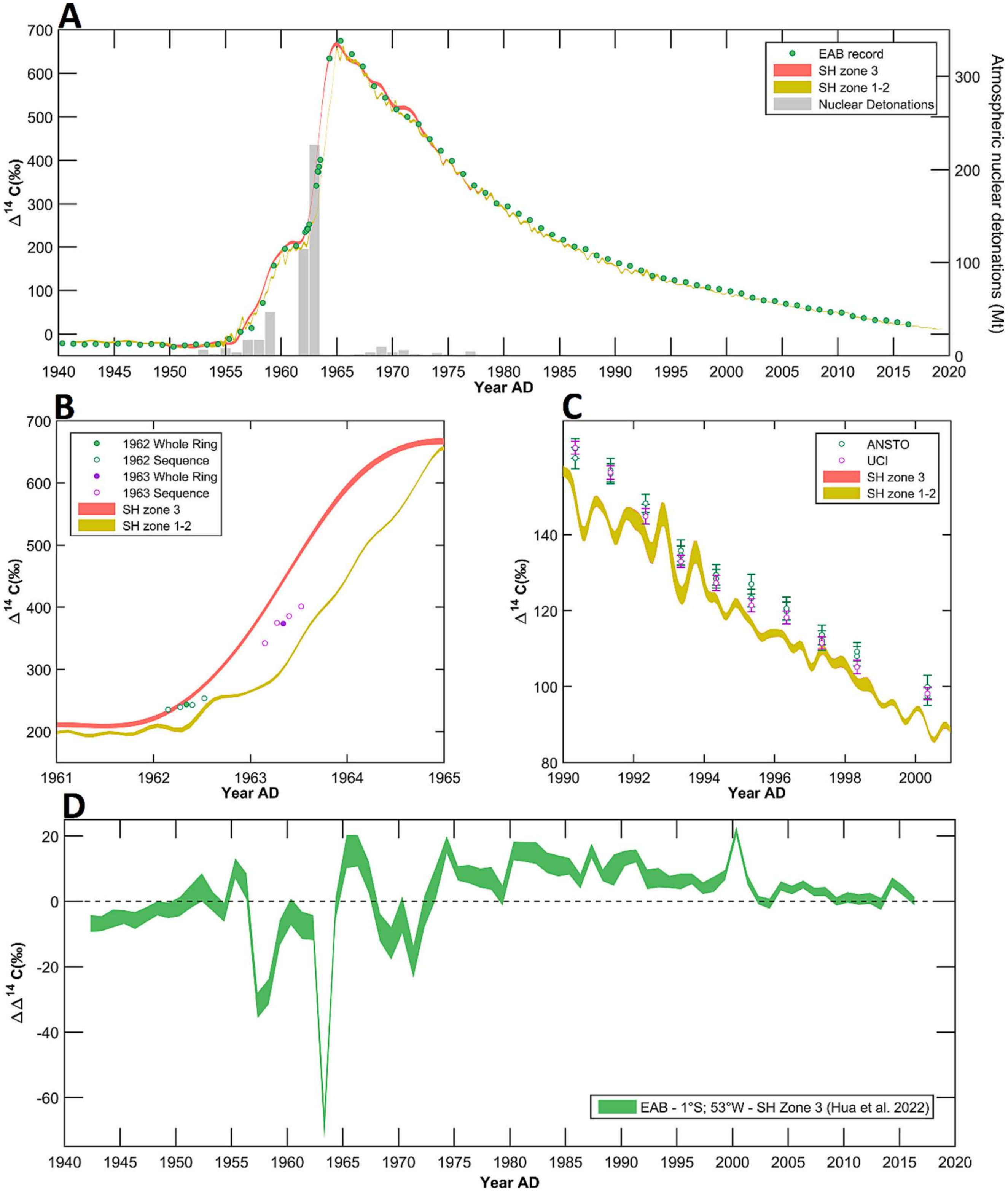

Fig. 4. The averaged Δ^{14}C values running from 1940 to 2016 of individual tree rings of *C. odorata* from the Eastern Amazon Basin (EAB; 1°S, 53°W) are shown, and have been compared with SH zonal compilation curves (Hua et al., 2022). The magnitude of nuclear detonations during the above bomb-testing period are also shown (gray bars – Enting, 1982) (A). To further evaluate *C. odorata* temporal growth at the site, ^{14}C levels of intra-annual succeeding-cuts from single tree rings belonging to the calendar years of 1962 and 1963 are compared with the ^{14}C levels of their whole tree-ring analogs of α-cellulose extracts produced by two labs, KCCAMS and LDEO (B). Accuracy of ^{14}C determinations of single tree rings were performed by an inter-laboratory comparison of ^{14}C results belonging to 1990–1998, and 2000 CE measured at the KCCAMS and ANSTO facilities (C). For $\Delta\Delta^{14}$C (EAB minus SH Zone 3) calculations, we used the same corresponding decimal calendar year fraction as of the EAB record (i.e., 0.34 yrs) (D).

November to April (Muna Island) differs notably from its position during the DJF months, when the TLPB typically reaches its southernmost extent over the SH.

Even though the EAB site is near the Amazon River, the GP back trajectories approaching the EAB for −24, −48, −72, −96, and −120 h (Fig. 5B) show that only a portion of the air masses from the Amazon River's mouth may reach our site during the growing season. This observation is significant because large ships using the Amazon River as a waterway to the Atlantic Ocean, burning fossil-fuels like diesel or crude oil, could potentially dilute atmospheric $^{14}CO_2$ locally, as demonstrated by Santos et al. (2022).

Although the percentages of interhemispheric air parcel contributions to the sites shown in Table 1 are approximate, they offer discernible amounts for expected outcomes from a given GP and hours in the past (i.e., the values displayed represent the total air mass percentages for a specific hour in the past as shown in the panels of Fig. 5A). The results from these percentage totals indicate that GP air mass contributions to the sites during tissue growth periods are consistently higher from the NH than the SH, aligning with the patterns of air flow near the equator during the austral summer (Wu et al., 2018).

The yearly −600 h back trajectory analysis (in %) of above sea level pressure for the EAB and Muna Island sites was conducted for the period between 1949 and 2016 (Fig. 6). As previously noted, NH air parcel contributions are significant to both sites during the study period. While air parcel contributions naturally fluctuate, a notable increase of approximately 5–10 % in NH air mass contributions to the EAB site was observed during the growth period of *C. odorata* (Fig. 6A, Table S1). Specifically, NH air mass contributions to the EAB site show a slight increase after the 1973 calendar year. In contrast, interhemispheric air mass contributions to the Muna Island site appear relatively stable throughout the study period, likely influenced by monsoon circulation in this region (Fig. 6B, Table S1), coinciding with the growth period of *T. grandis*. This finding suggests the need for further research into recent changes in interhemispheric air masses.

3.3. Fine-tunning observations for the tree-ring EAB ^{14}C dataset

Radiocarbon concentrations have a complex relationship within distinct reservoirs. Some reservoirs, such as the atmosphere and biomass, can fast-cycle ^{14}C (Hua et al., 2022). Others, such as the oceans (e.g., Aramaki et al., 2001; Wagner et al., 2009) and soils (e.g., Harrison, 1996; Carrasco et al., 2006) cycle ^{14}C slowly. In our discussions, we will take into account influence of air masses as well as possible carbon reservoir inter-relationships. In Fig. 7, various aspects of ^{14}C concentrations over the EAB from the pre- to post-bomb period are presented. This figure compares EAB tree-ring ^{14}C values with stand-alone ^{14}C records within SA and compiled SH zone 3 ^{14}C data as $\Delta\Delta^{14}C$ (‰). The distinct panels in the figure represent different calendar year ranges and independent ^{14}C records, with panels B and C showing some overlapping years.

3.3.1. The pre-bomb era (before 1955 CE)

During the pre-bomb era, before the onset of atmospheric bomb radiocarbon around 1955 CE, the period was mainly characterized by smaller temporal atmospheric $\Delta^{14}C$ variations, as noted by Kutschera (2022). Lower than expected pre-bomb ^{14}C levels, influenced by fossil CO_2 burning, were detected through ^{14}C tree-ring analyses from various locations in both hemispheres (Levin et al., 2010 and references therein). The emissions of fossil CO_2, containing ^{14}C-free values, in conjunction with anthropogenic activities since the Industrial Revolution, significantly influenced atmospheric $\Delta^{14}C$ variability worldwide. This was due to the dilution of atmospheric ^{14}C by the input of ^{12}C and ^{13}C, known as the Suess effect (Suess, 1955). However, this signal was overshadowed by the substantial input of $^{14}CO_2$ from nuclear bomb ^{14}C production in the mid-20th century. In this context, the short pre-bomb EAB ^{14}C data running from 1940 to 1955 do not show significant dilution in ^{14}C when compared with the SH zone 3 compilation of Hua et al. (2022) (Fig. 4A), and even less so when compared against stand-alone tropical and subtropical SA ^{14}C records, specifically Porto Trombetas, Central Amazon (1°S, 56°W; Santos et al., 2022) and Camanducaia, Brazil (22°S, 46°W; Santos et al., 2015) (Fig. 7A). Therefore, the contribution of pre-bomb era fossil CO_2 does not appear to be significant in the tropics during this short period.

3.3.2. The early and rising portion of the bomb period

The EAB tree-ring ^{14}C data from 1955 to 1960 shows a slightly lower $\Delta^{14}C$ bomb signal compared to the SH zone 3 dataset (Fig. 4A). We explored this pattern by plotting in Fig. 7B both the EAB tree-ring ^{14}C data and the Porto Trombetas data (1°S, 56°W; Santos et al., 2022) as $\Delta\Delta^{14}C$ (‰), using the SH zone 3 curve (which during this time-period is solely based on the Muna Island dataset - 5°S, 122°E; Hua et al., 2012) as reference. We believe that those lower atmospheric $\Delta^{14}C$ values in the Amazon Basin reflect the negative ^{14}C isoflux effect on tropospheric air over large land-biomass areas, as modeled by Randerson et al. (2002). Early bomb ^{14}C age profiles of soils typically show pre-bomb signals that were incorporated thousands to decades earlier (e.g., Trumbore and Zheng, 1996; Harrison, 1996). From this understanding, it is reasoned that the Amazon rainforest floor and its vegetation released older ^{14}C, while new biomass tissue was still been tagged by excess bomb ^{14}C (Figs. 4A and 7B). To some degree, it is possible that the Atlantic Forest acted in the same fashion. For instance, the Camanducaia record (22°S, 46°W; Santos et al., 2015), located in the Atlantic Forest biome of southeastern Brazil's highlands, shows tree-ring ^{14}C values from the native *Araucaria angustifolia* tree are slightly lower (Fig. S4A) than the SH zone 1–2 compilation for 1955–1960 (Hua et al., 2022). The Irruputuncu site (20°S, 68°W; Ancapichún et al., 2021), at a similar latitude to Camanducaia but in a high mountain ecosystem (Fig. S4B), shows air parcel contributions dominated by the extratropical Pacific Ocean, followed by the Amazon Basin and upper atmosphere (Ancapichún et al., 2021). This mix of air parcel contributions could also explain the $\Delta^{14}C$ bomb signal differences between these sites, in addition to the type of forest cover.

Air-sea $\Delta^{14}C$ contributions from the Mauritania-Senegalese upwelling region off the northwestern African coast, which intensifies in March (Gallego et al., 2021), leading to air masses from the African coast being transported across the Atlantic Ocean to the EAB (Fig. 5), cannot be excluded. Direct ^{14}C measurements off the northern African coast reveal relatively low $\Delta^{14}C$ values in surface waters and shells (Nydal et al., 1998; Ndeye, 2008), attributed to the Antarctic Circumpolar Current (ACC) bringing ^{14}C-aged deep water across the Atlantic Ocean (e.g., Broecker et al., 1960; Fairhall and Young, 1985) to the surface near upwelling zones (Toggweiler et al., 2019). Although subantarctic degassed low air-sea $\Delta^{14}C$ values may continue to reach surface waters north of the ACC, their contributions to the EAB, if any, were likely obscured by the rapidly increasing $^{14}CO_2$ from nuclear bomb ^{14}C production during this period.

While the impact of biosphere negative ^{14}C isoflux may be negligible at Muna Island, given the comparatively smaller combined rainforest areas in Southeast Asia than in the Amazon Basin, air masses reaching the island are partly from the easternmost region of Asia and the tropical and subtropical Pacific Ocean (Fig. 5A). Additionally, Muna Island's proximity to nuclear detonation sites in the North Pacific (<20° away; Enting, 1982 - Fig. 5A) cannot be overlooked. Regions influenced by monsoon circulation, such as the Asian maritime continent, are likely to exhibit air mass isentropic flow (Yan et al., 2019) and enhanced isotopic signals (Randel and Park, 2006), including bomb ^{14}C.

Between 1961 and 1964, the EAB $\Delta^{14}C$ data from both whole-rings and intra-annual wood slices align closely with the SH zone 1–2 and zone 3 curves of Hua et al. (2022), as shown in Fig. 4A and highlighted in 7B. But data is not equal to those in either SH zone 1–2 or zone 3 curves. The EAB $\Delta^{14}C$ values for whole-rings are averaged results from replicates of α-cellulose fibers obtained from LDEO and UCI, making sample

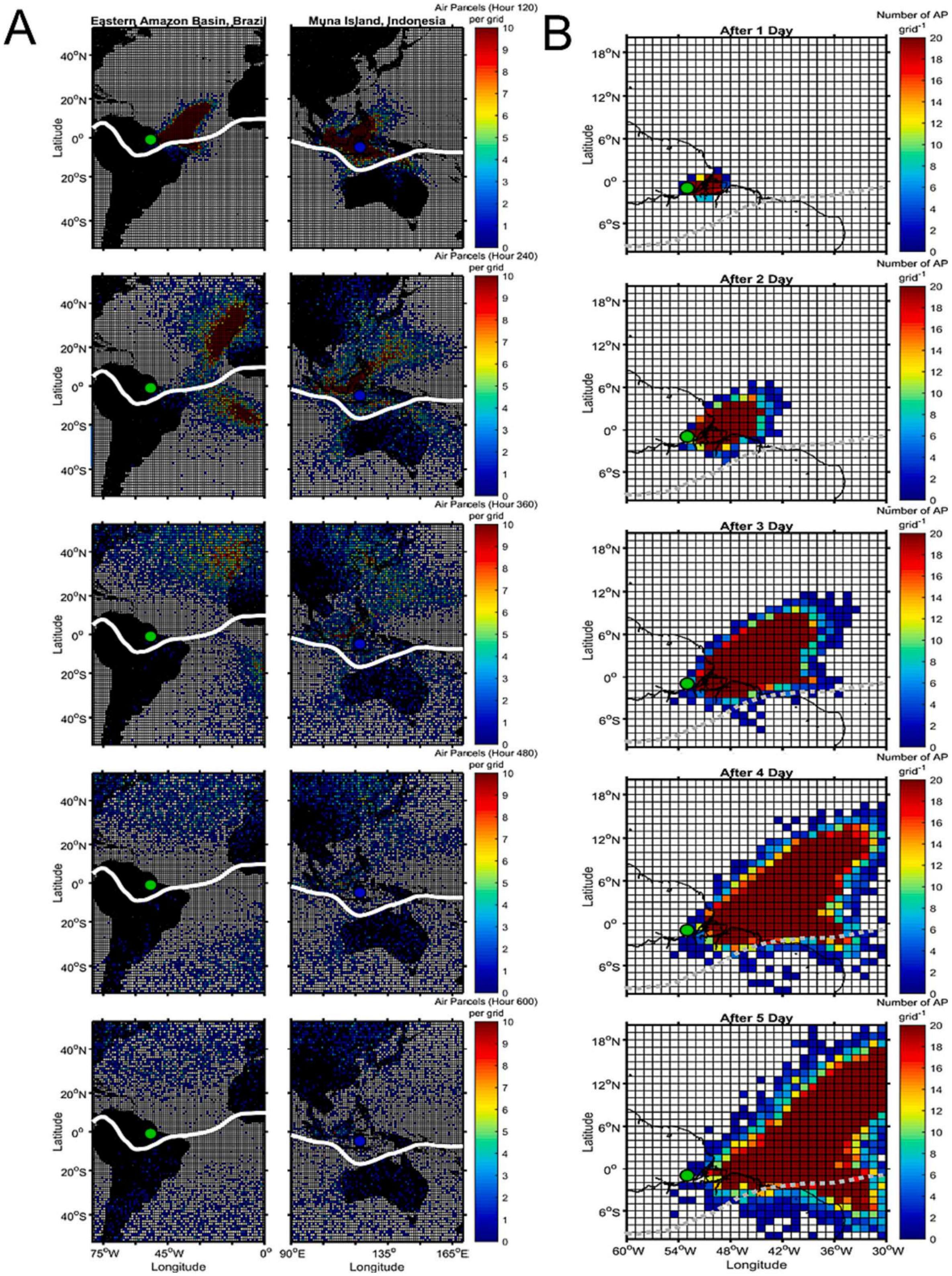

Fig. 5. HYSPLIT backward trajectory analysis results for: (A) The past hours of −120, −240, −360, −480, and −600 (top to bottom panels) during 1949 to 2016, and reaching the either EAB (Feb to Jul when *C. odorata* was growing – left panels) or Muna Island, Indonesia (Nov to Apr when *T. grandis* was growing – right panels). Solid white line displayed in panels roughly shows the mean temporal shape of the TLPB for the month periods disclosed above. To see the average percent totals from the NH and SH of each panel, refer to Table 1. (B) The past hours of −24, −48, −72, −96 and −120 (top to bottom panels) during 1949 to 2016, and reaching the EAB endpoint. The color bar scale in all time windows indicates the density of the GP air parcels located on each pixel grid, i.e., the 1° × 1° grid encapsulated in the black grid lines on images (80:100 for Fig. 5A, and 30:30 for Fig. 5B).

Table 1

Averaged percentages of NH and SH contributions of air parcels that arrived at the EAB and Muna Island sites, and were captured by the tree species of *C. odorata* and *T. grandis*, respectively. Those values are associated with the GPs displayed in Fig. 5A and described in the main text.

Destination site	Input	Hour – 120	Hour – 240	Hour – 360	Hour – 480	Hour – 600
EAB	NH	93.07 ± 5.7	72.53 ± 9.08	70.62 ± 8.76	70.4 ± 8.81	70.4 ± 8.73
	SH	6.92 ± 5.7	27.46 ± 9.08	29.37 ± 8.76	29.59 ± 8.81	29.59 ± 8.73
Muna Island	NH	94.02 ± 4.13	78.88 ± 7.44	72.25 ± 8.38	69.38 ± 8.8	68.19 ± 8.99
	SH	5.97 ± 4.13	21.11 ± 7.44	27.74 ± 8.38	30.61 ± 8.8	31.8 ± 8.99

mishandling unlikely. Additionally, the Δ^{14}C values from wood slices produced at UCI from new wood cuts also align similarly with their whole-ring counterparts. The EAB Δ^{14}C data centered around early April of 1962 and 1963 closely matches the Porto Trombetas ^{14}C record (Fig. 7B), located 3° west of the EAB. Given the overlapping tree growth periods of *Hymenolobium petraeum* in Porto Trombetas and *T. grandis* in Muna Island, it is unlikely that $\Delta\Delta^{14}$C offsets between the EAB and Muna are due to differences in tissue growth timing. Moreover, the fact that these ^{14}C offsets appear on just those ^{14}C records influenced by the Amazon rainforest (the EAB and Porto Trombetas), but not to the Camanducaia record in the Atlantic rainforest (in Santos et al., 2015) implies that the effect cannot be solely credited to terrestrial carbon fluxes carrying negative ^{14}C values. The observed Δ^{14}C differences are likely related to the source and destination of air parcels loaded with high levels of $^{14}CO_2$ as they crossed the equatorial line following major detonations.

Cross-equatorial transport in the TLPB region from the NH extra-tropical upper stratosphere is complex, following different pathways from east to west (the Pacific and Atlantic westerly ducts; Yan et al., 2021). Although the Asian Monsoon circulation is a major driver for inter-hemispheric transport (Yan et al., 2019, 2021), the seasonal air flow reaching the EAB region is expected to arrive slightly later than that reaching Muna Island. Therefore, distinct excess-^{14}C levels from the NH, after atmospheric mixing with $^{14}CO_2$ from other GPs (Fig. 5A), may partly explain the differences detected between EAB and Muna Island datasets from 1961 to 1964. This suggests that longitudinal asymmetry among sites at nearly the same latitude but on opposite sides of the globe (EAB versus Muna Island) has been detected.

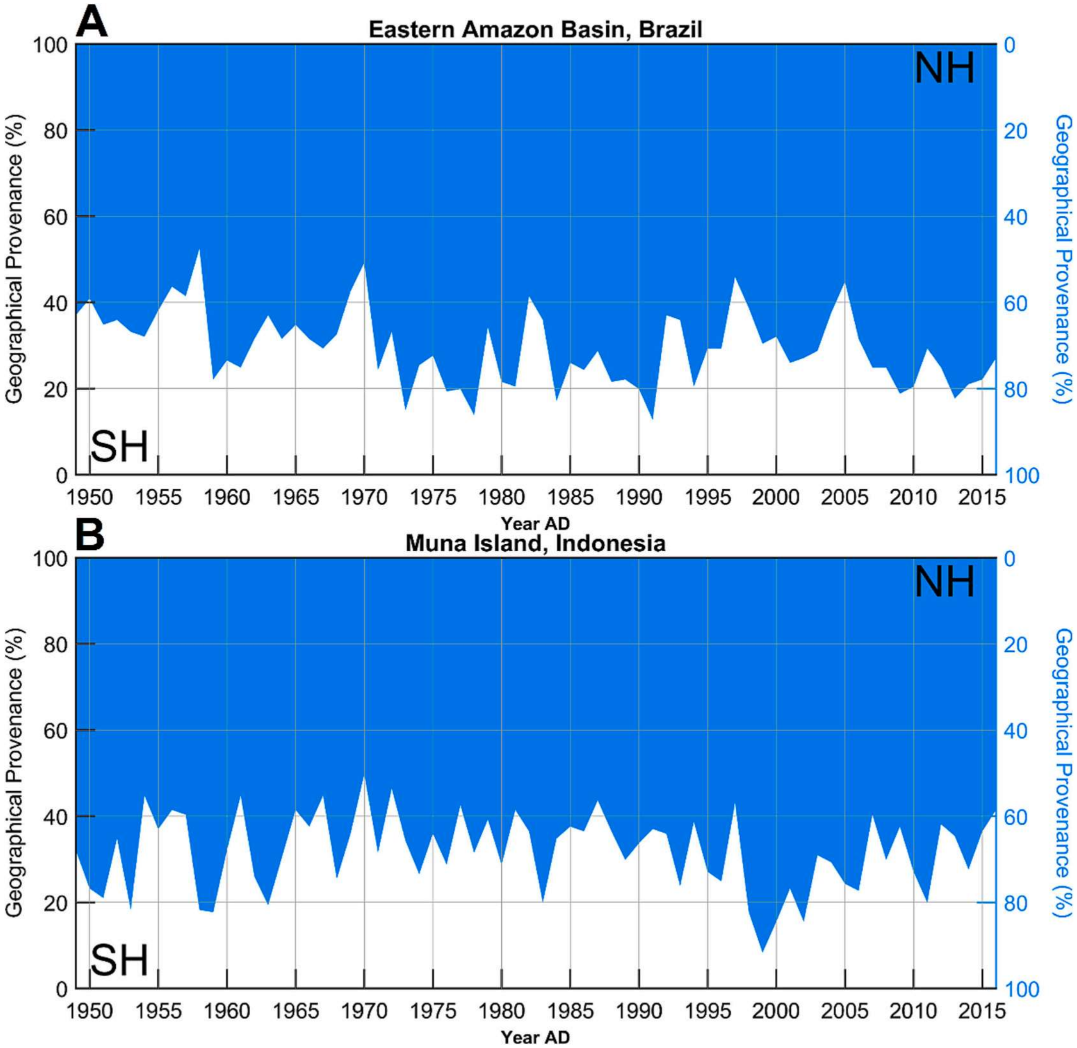

Fig. 6. Air parcel contributions (in %) of −600 h arriving at the EAB site between Feb and Jul (A), and the Muna Island site between November and April (B) from 1949 to 2016. Blue area corresponds to air parcel contributions from the Northern Hemisphere (NH), while the white area reflects those from the Southern Hemisphere (SH).

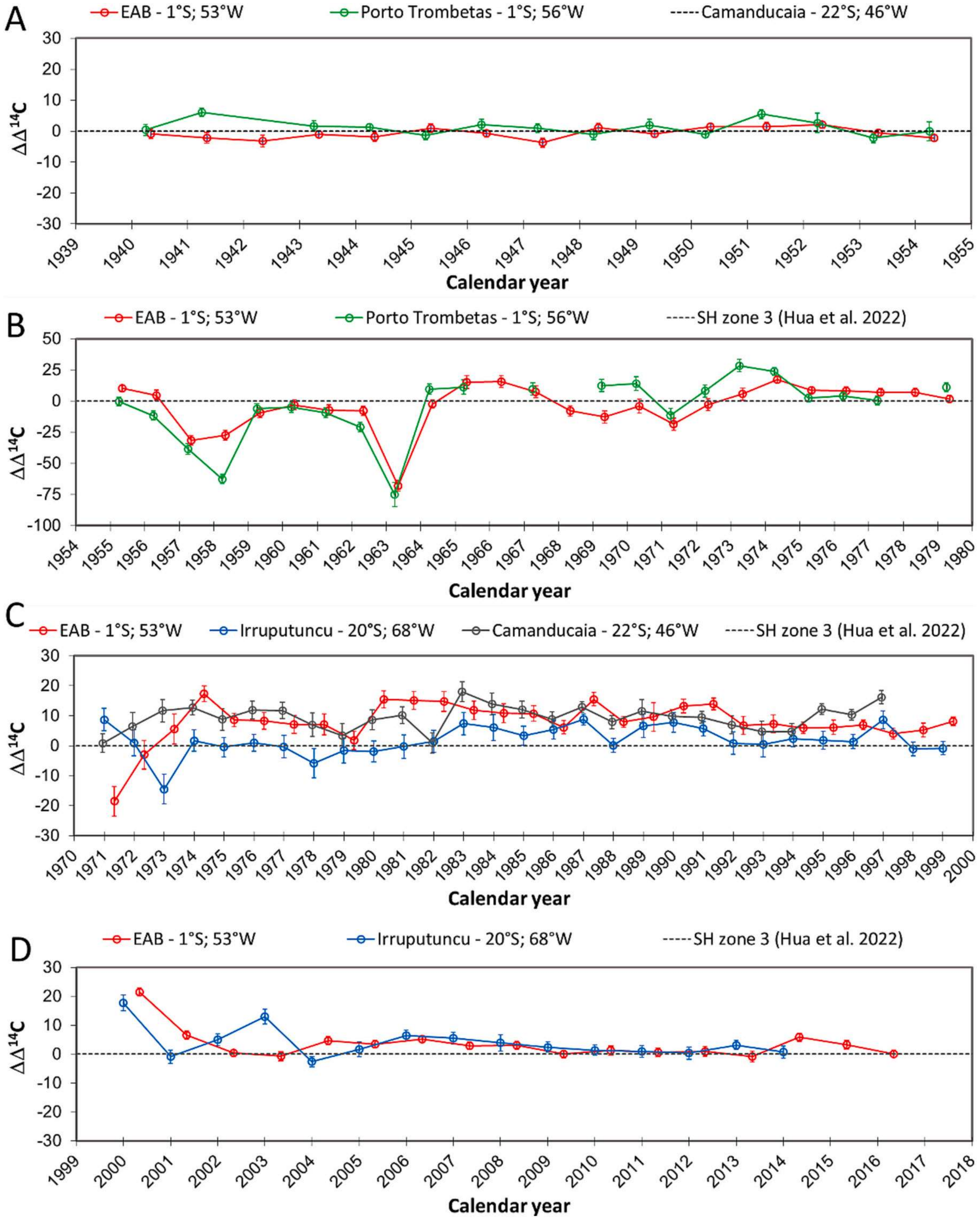

Fig. 7. Comparison of observed tree-ring EAB ^{14}C values, stand-alone records in SA and compiled SH ^{14}C data as $\Delta\Delta^{14}$C (‰) during the pre-bomb (A), bomb-pulse (B), post-bomb (C), and most recent periods (D). A 60 ‰ y-axis range was chosen for most panels, except panel B (150 ‰). For $\Delta\Delta^{14}$C calculations among records, we used the same corresponding decimal time fraction of the reference record (i.e., 0.34 yrs to EAB, and 0.01 yrs to Camanducaia and Porto Trombetas). When the Camanducaia record was used as reference (panel A), we assumed that ^{14}C levels between 0.34 yrs from EAB and 0.01 yrs from Camanducaia were somewhat compatible.

3.3.3. The bomb maximum period

From 1964 to 1970, the EAB tree-ring ^{14}C record accurately reflected the peak levels of bomb-produced ^{14}C, aligning with the signatures from the most powerful nuclear detonations that exceeded 20,000 ‰ in Δ^{14}C in the Stratosphere (Levin and Hesshaimer, 2000). For example, the early 1964 Δ^{14}C value from the EAB (shown in Fig. 4A) is essentially consistent with the SH zone 3 compilation, which includes the Muna Island record, as depicted in Fig. 7B. This period marks a phase where the ^{14}C signatures in the EAB region had effectively synchronized with the highest levels of ^{14}C produced by nuclear detonations.

In April 1965, the EAB tree-ring ^{14}C record reached its highest value, showing a Δ^{14}C of 674 ± 2 ‰ ($n = 2$). This value is slightly higher than the Δ^{14}C of 667.1 ± 4.5 ‰ recorded for Muna Island and the Δ^{14}C of 670.3 ± 3.2 ‰ ($n = 6$) for Porto Trombetas, both of which are sites near the Equator (Table 2). Overall differences among the ^{14}C results of these three sites near the equatorial line is not statistically significant within error. We expect that the continuous improvements to analytical instrumentation and sample handling for atmospheric ^{14}C reconstructions (Bronk Ramsey, 2023) would lead to gradually more precise ^{14}C information in the future, so that small differences become meaningful. Still, the Δ^{14}C value observed in the atmosphere at the EAB during the bomb-peak aligns with other tree-ring ^{14}C measurements across the SH. Notably, starting from the EAB, which is near the Equator, there is a discernible decrease in the Δ^{14}C gradient across various locations between 1965 and 1966, as shown in Table 2. This indicates that the highest Δ^{14}C value in the region from the SH to the equatorial line likely occurred between January and May of 1965. This peak Δ^{14}C value has been identified in the wood tissue of *C. odorata* trees at the EAB, as reported in this study.

Levin et al. (2022) estimated the NH to SH ^{14}C time-lag at approximately 1.4 years, based on maximum Δ^{14}C-CO$_2$ values at specific midlatitude sites, aligning with midlatitude inter-hemispheric transport times for other gases like sulfur hexafluoride (SF6) as noted by Waugh et al. (2013). However, Hua et al. (2012) suggested a faster transport of bomb Δ^{14}C-CO$_2$, from 0.5 to 1 year, from northern temperate regions to the tropics. To evaluate these inferences, Fig. S5 plots a sequence of compiled Δ^{14}C values from the intra-hemispheric geographical division of Hua et al. (2022) and tree-ring Δ^{14}C results from the EAB site. The analysis shows that the inter-hemispheric time lag between NH1 and SH3 is over 1.5 years, longer than the approximately 0.5-year lag between NH3 and SH3. However, the time lag for Δ^{14}C-CO2 transfer between NH3 and EAB seems closer to 1 year, especially considering the highest value for SH low latitude in the 1965.34 calendar year AD (Table 2). Future ^{14}C-AMS results from subsequent cuts of single tree rings from the calendar years 1964, 1965, and possibly 1966 CE from multiple locations within the TLPB should provide more precise insights into the inter-hemispheric transport of bomb ^{14}C.

3.3.4. *The post bomb period*

After the 1965 bomb peak, the EAB record shows the expected decline in atmospheric Δ^{14}C values (Fig. 4A), aligning with the Nuclear Test-Ban Treaty of September 1963 and the subsequent redistribution of excess-^{14}C across the geospheres (atmosphere, ocean, biosphere). However, from the mid-1970s onwards, the EAB ^{14}C dataset remains slightly higher than the SH zone 3 compilation by Hua et al. (2022) (Fig. 4D). It is important to note that Hua et al. (2022) used the same datasets for zone 1–2 compilation to maintain continuity in SH zone 3 compilation post-1979 (footnote of Fig. 1). The timing of tree-ring growth at the EAB, confirmed by ^{14}C results from intra-annual wood slices (Fig. 4B), eliminates the possibility of calendar year displacement affecting our record. Additionally, the EAB record includes numerous ^{14}C replicates and inter-laboratory analyses of raw wood cuts pretreated and measured at UCI and ANSTO (Figs. 3C and 4C), ruling out sample and measurement errors. Enriched ^{14}CO$_2$ contributions from fires related to deforestation and waste clearing are also unlikely. While deforestation in the Amazon Basin occurs almost year-round, fires are concentrated in the dry season (July to October; Morgan et al., 2019). Airflow from the NH crossing the Equatorial Atlantic Ocean towards the EAB from February to July is mostly from northeast (NE) direction (Fig. 5B), eventually flowing to the southeast region of the continent (Botía et al., 2022). Consequently, smoke clouds from the Southern Amazon Basin typically dissipate towards the southwest and southeast of SA, where they are later detected in Brazilian southeast metropolitan cities (Andela et al., 2022). Therefore, the possibility of Amazon Basin ^{14}CO$_2$ fires significantly biasing the EAB ^{14}C record is not considered plausible.

The EAB record suggests a shift from a net sink to a source of bomb ^{14}CO$_2$ after 1970, with captured bomb carbon being re-emitted by litter and soils and then reabsorbed by vegetation (Fig. 7C). This aligns with the positive atmospheric Δ^{14}C anomaly reported by Levin and Hesshaimer (2000), Randerson et al. (2002), and Naegler and Levin (2009). A similar post-bomb biocarbon enrichment is observed in the early 1970s in the Porto Trombetas tree-ring ^{14}C record (Santos et al., 2022 - not shown in Fig. 7C). However, this effect was obscured from the 1980s onwards due to fossil-fuel burning associated with mining operations and extensive shipping networks in west-central Pará State, utilizing the Amazon River to the Atlantic Ocean. The bomb ^{14}C enrichment effect is also evident in the Camanducaia tree-ring ^{14}C record (Fig. 7C), located in the Brazilian Atlantic moist forest bioregion (Fig. 1) and influenced by the South Atlantic Convergence Zone (SACZ) during the Austral summer (Zilli et al., 2019; Fialho et al., 2023). The combined effect of extratropical Atlantic Ocean air masses and high ^{14}C fluxes from land appears to be the primary cause of increased ^{14}C values in records along the SA Atlantic coast, including the EAB (this study) and Camanducaia sites (Santos et al., 2015). This suggests that the time ^{14}CO$_2$ remains over the Amazon Basin, before being assimilated as biomass, is enough to be altered by the ecosystem's carbon isotopic signature. The apparent biosphere disequilibrium, primarily due to bomb-pulse carbon feedback, seems to be the sole mechanism for the enrichment of 5 to 15 ‰ in the EAB ^{14}C record from 1970 to 2000 (Fig. 7C). Even though, measured age-depth profiles show that Δ^{14}C values tend to vary significantly with soil taxonomy and decrease fast in tropical forests through the first meter, the bulk surface of respired data in tropical ecosystems show a release of positive Δ^{14}C values after the bomb peak maximum compared to boreal, temperate and tundra ecosystems (Blackaby, 2022 and references therein).

In contrast, the Irruputuncu tree-ring ^{14}C record, at a similar latitude to the Camanducaia site, shows a notably lower ^{14}C signature during this period, likely due to its Altiplano location. Ancapichún et al. (2021) found that the Irruputuncu tree-ring ^{14}C record has a distinct bomb-

Table 2

Radiocarbon tree-ring data from multiple locations in the SH for the calendar years of 1965 and 1966. Results are shown as age-corrected Δ^{14}C (‰), and is displayed from low to high latitude to facilitate on discussions.

Sample/location	Coordinates	Calendar year AD	Δ^{14}C (‰)	±1σ	#	Citation
Cedrela Odorata, EAB, Brazil	1°S, 53°W	1965.34	674.4	2.0	2	This study
		1966.34	644.0	1.6	3	
Hymenolobium petraeum, Central Equatorial Amazon, Brazil	1°S, 56°W	1965.25	670.3	3.2	6	Santos et al. (2022)
		1966.25*	n/a	n/a	n/a	
Tectona grandis, Muna Island, Indonesia	5°S, 122°E	1965	667.1	4.5	1	Hua et al. (2012)
		1966	633.7	5.2	1	
Polylepis tarapacana, Irruputuncu, Altiplano, Chile	20°S, 68°W	1965	627.5	3.1	1	Ancapichún et al. (2021)
		1966	633.5	3.2	1	
Agathis australis, Baring Head, New Zealand	41°S, 174°E	1965	532.9†	3.2	1	Turnbull et al. (2017)
		1965	577.4	3.3	1	
		1966	610.9	3.3	1	

[#] Refer to the number of measurements averaged, when applicable.

[*] The calendar year was unsampled (wedging ring in both radii – see details in Santos et al., 2022).

[†] Δ^{14}C value is too low, and most likely unreliable due to wood sampling. See details in Turnbull et al. (2017).

pulse with a continent-ocean carbon mixture of approximately 25 % Amazon Basin air mass contributions, 55 % from the Pacific Ocean, and 15 % from the upper troposphere. This underscores the impact of longitudinal asymmetry among sites and the significance of GP air masses on ^{14}C fluctuations.

The anticipated release of enriched ^{14}C from the terrestrial biosphere, as predicted by models (Levin and Hesshaimer, 2000; Randerson et al., 2002; Naegler and Levin, 2009), was expected to begin two to three decades after the last aboveground nuclear detonations of the 1960s. However, direct ^{14}C measurements from tree rings in the EAB record indicate that this re-emission commenced much earlier, in the 1970s (Figs. 4A and 7C), and persisted for an extended period, lasting until the early 2000s.

3.3.5. *The fossil fuel and current era*

Since the early 2000s, the ^{14}C data from the EAB has shown a significant decrease, aligning with the subtropical atmospheric record from Cape Matatula, American Samoa (14°S, 171°W; 2001–2007; Graven et al., 2012), and the tree-ring record from Irruputuncu in the Altiplano (20°S, 68°W; 1950–2014; Ancapichún et al., 2021) (Fig. S6). This recent EAB ^{14}C data also closely matches the SH zone 3 compilation by Hua et al. (2022), despite this compilation was mostly built from mid- to high-latitude dataset sites in the Southern Hemisphere (Fig. 1). To understand this trend, we propose several broad topics for future discussion and research.

One factor considered by Turney and Palmer (2007) on pre-bomb interhemispheric ^{14}C offset variability is the influence of the El Niño-Southern Oscillation (ENSO). ENSO events originate in the tropical Pacific, and often have a strong effect on the western coast of SA (Brienen et al., 2012). When evaluating atmospheric $\Delta^{14}C$ data from Wellington, New Zealand (41°S, 174°E), Dutta (2002) proposed that ENSO events could significantly impact tropical CO_2 fluxes in the post-bomb period. According to Dutta's interpretation in the (2002) work, $^{14}CO_2$ air-sea exchange fluxes during ENSO events should lead to a positive ^{14}C anomaly in the atmosphere over land. However, considering the rapid and continuous decrease in the EAB $\Delta^{14}C$ after 2000, ENSO does not appear to be a plausible explanation for this trend.

It is conceivable that as global bomb $\Delta^{14}C$ values declined over time, the positive ^{14}C fluxes from the Amazon Basin to the EAB site also diminished. Indeed, ^{14}C data from tropical surface soil profiles (0–30 cm; Lawrence et al., 2020) in 2000 is about tenfold smaller in magnitude (7 ‰ in average, and maps in Shi et al., 2020) than of that from previous decades (e.g., Harrison, 1996). With the reduced impact of local positive-$\Delta^{14}C$ biocarbon influx, the influence of air-sea contributions from the Mauritania-Senegalese upwelling region, known for its low-$\Delta^{14}C$ values, might become more apparent. However, Toggweiler et al. (2019) observed that the $\Delta^{14}C$ differences across ocean basins during 2003 to 2005 were smaller compared to previous decades, due to the penetration of the bomb $\Delta^{14}C$ signal into the oceans. Therefore, the hypothesis that low-$\Delta^{14}C$ contributions from deep ocean waters surfacing in the upwelling zones off northwestern Africa and reaching the EAB site are responsible for the observed decrease (or its similarity to datasets of SH zone 1–2) in $\Delta^{14}C$ values in the 2000s seems unlikely. Hence, we do not expect large effects from either respired land carbon or air masses from upwelling regions between 1990 and 2016, especially to the EAB site.

Our −600 h back trajectory analysis for the EAB site over time (Fig. 6A) revealed a 5 to 10 % increase in air-mass contributions from NH sources (Table S1). This observation leads us to suspect a long-term increase in fossil-fuel levels over SA as a potential cause for the sudden decrease in the EAB site's ^{14}C signature after 2000. The anticipated influence of fossil CO_2 emissions, stemming from continuous fossil fuel combustion, cement manufacturing, and alterations in land use (Friedlingstein et al., 2022, 2023), was expected to contribute to a reduction in the ^{14}C values of atmospheric CO_2 across both hemispheres starting from the 1990s (Turnbull et al., 2017; Levin et al., 2022). Although terrestrial biosphere enrichment in ^{14}C at the EAB site persisted until the early 2000s (Fig. 7D), recent data (2014–2019) from the Amazon Tall Tower Observatory (ATTO) at 2.1°S and 58.9°W indicate that the inter-annual variability of net ecosystem exchange in eastern Amazonia is primarily influenced by vegetation (Botía et al., 2022). This biosphere disequilibrium may have initially obscured the detection of NH fossil CO_2 intrusion in the EAB ^{14}C record during the 1990s. However, as the average atmospheric $\Delta^{14}C$ in the SH decreased from 674 ± 2 ‰ in 1965 (Fig. 4A) and the Amazon Basin's biosphere disequilibrium began to wane, we speculate whether the Amazon Basin became more reflective of the effects of fossil-fuel $^{14}CO_2$ dilution, coinciding with an increase in fossil-fuel CO_2 intrusion from NH energy-related emissions. The NH anthropogenic CO_2 increase was 9 PgC from the 1980s to 1990s and surged another 15 PgC from the 1990s to 2000s (Ciais et al., 2019). Recent CO_2 concentration data (2014–2019) from Botía et al. (2022) at ATTO showed a steady average increase of 2.38 ppm year^{-1}, slightly lower than the global mean CO_2 growth rate of 2.49 ± 0.08 ppm year^{-1} for the same period (Dlugokencky and Trans, 2020). Furthermore, Botía et al. (2022) demonstrated that CO_2 concentration data is seasonally driven, peaking during the wet season when most trees in the Amazon Basin, including *C. odorata* at the EAB, are growing (Fig. 1). Although this CO_2 is not solely derived from fossil fuels, it is plausible to assume that the low $\Delta^{14}C$ values detected at the EAB after 2000 are indeed caused by fossil-fuel $^{14}CO_2$ intrusion from the NH.

Other potential atmospheric ^{14}C sources with lower $\Delta^{14}C$ values, originating from low-latitude regions, should also be considered (Fig. 5A). Wiggins et al. (2018) documented relatively low ^{14}C levels from smoke plumes of fires and smoldering in Southeast Asian tropical peatlands, which can spread across a broad area between 7°S and 5°N (Thampi et al., 2009). Additionally, significant CO_2 emissions from peat burning have been reported in other Asian regions and the Northern Hemisphere (Houghton and Castanho, 2023). However, direct ^{14}C measurements of these emissions are yet to be conducted, which would provide insights into their ^{14}C signatures and global impact.

In Fig. 8, we then evaluate the decline of bomb ^{14}C at the EAB site by two modes. At first, we observed the trend of the global fossil fuel atmospheric CO_2 estimates (Friedlingstein et al., 2023) and how it may have impacted the EAB $\Delta^{14}C$ values from 1966 onward (Fig. 8A). For the sake of comparisons with NH and SH compilation data (Hua et al., 2022), we then break down the decline of bomb ^{14}C at the EAB site into two periods, i.e., 1971 to 2000 (Fig. 8B) and 2001 to 2016 (Fig. 8C). Researchers have been using the decay constant ($T_{1/2}$) of the exponential function of atmospheric records after the bomb-maximum period as an indicator of the rate of ^{14}C changes due to terrestrial and oceanic sinks, and/or fossil fuel input (e.g., Park et al., 2002; Xiong et al., 2021). We determined that the EAB record was decreasing exponentially between 1971 and 2000 with a $T_{1/2}$ of 17.5 years. Our estimate is overall in alignment with the $T_{1/2}$ of 16.7 years for the SH zone 1–2 compilation of Hua et al. (2022), which utilize several datasets from mid- to high-latitudes in the SH.

Assuming that fossil CO_2 emissions in the global atmosphere are largely responsible for the bomb ^{14}C changes from the middle 1990s onward (Levin et al., 2022), where it had already surpassed the 25 BMT mark (Fig. 8A), we then evaluated the decline of bomb ^{14}C at the EAB site from 2001 to 2016 (Fig. 8C). The latter time-frame was chosen due to the observed drop in $\Delta\Delta^{14}C$ (‰) between 2000 and 2001 in the EAB record (Fig. 7D). From 2001 to 2016, the decline of the EAB ^{14}C record is basically linear as well as other datasets in the NH and SH (Fig. 8C). For comparisons, we used the ^{14}C data between February to July (the growth period of *C. odorata* at the EAB site) of the NH zone 2 compilation as well as SH zone 1–2 of Hua et al. (2022), as those compilations are more complete in terms of ^{14}C datasets than NH zone 3 and SH zone 3, respectively. The average $\Delta^{14}C$ rate of decrease for the EAB site as well as those ^{14}C records from mid-latitude of NH regions is basically the same (∼4.5 ‰ per year), while for SH mid- to high-latitudes records we obtained ∼4.4 ‰ per year. The similarity between $\Delta^{14}C$ decrease rates for the EAB and sites further north would indicate an enhancement of fossil fuel CO_2 directed to our site between 2001 and 2016. Since the EAB ^{14}C record was produced from a pristine area in terms of point-source pollution, fossil fuel CO_2 reaching this site must be from a nonpoint source, such as air masses crossing the equatorial line (Fig. 5A).

Next, we present the annual decline in $\delta^{13}C$ values from the EAB (1940–2016) and Porto Trombetas (1938–2007) sites (Fig. 8D), based on EA-IRMS measurements of the remaining cellulose fibrils, as detailed in Section 2.3.4. While tree-ring $\delta^{13}C$ data can also include physiological and climatic responses, here we are just interested on evaluating its general decline due to decrease in $\delta^{13}C$ atmospheric composition. Time-series in Fig. 8D show a gradual and similar decline in $\delta^{13}C$ values, indicating fossil-fuel dilution rates of 0.020 ‰ per year for EAB and 0.026 ‰ per year for Porto Trombetas. Given that both sites predominantly receive air flow from the northeast, with a small contribution from southeast (Fig. 5B), the isotopic dilutions observed in both ^{14}C (Fig. 7D) and $\delta^{13}C$ (Fig. 8D) are likely influenced by contributions from the Northern Hemisphere and the equatorial Atlantic Ocean (Fig. 5A). Notably, the dilution rate at the Porto Trombetas site, located deeper within the Amazon Basin, is higher. This increased rate, particularly from 1980 to 2007 (0.033 ‰ per year, as shown by the black dashed line in Fig. 8D), is attributed to local fossil fuel CO_2 emissions from mining operations in Pará State (Santos et al., 2022). Consequently, the $\delta^{13}C$ series also supports that the EAB site has been impacted by global fossil fuel emissions during the current era.

The notable alignment of our EAB ^{14}C record, situated at lower latitudes, with other records from further south represents a significant and unique observation in the field of atmospheric ^{14}C studies. This finding underscores the need for more comprehensive research. To fully understand and clarify these complex patterns, it is essential to establish a

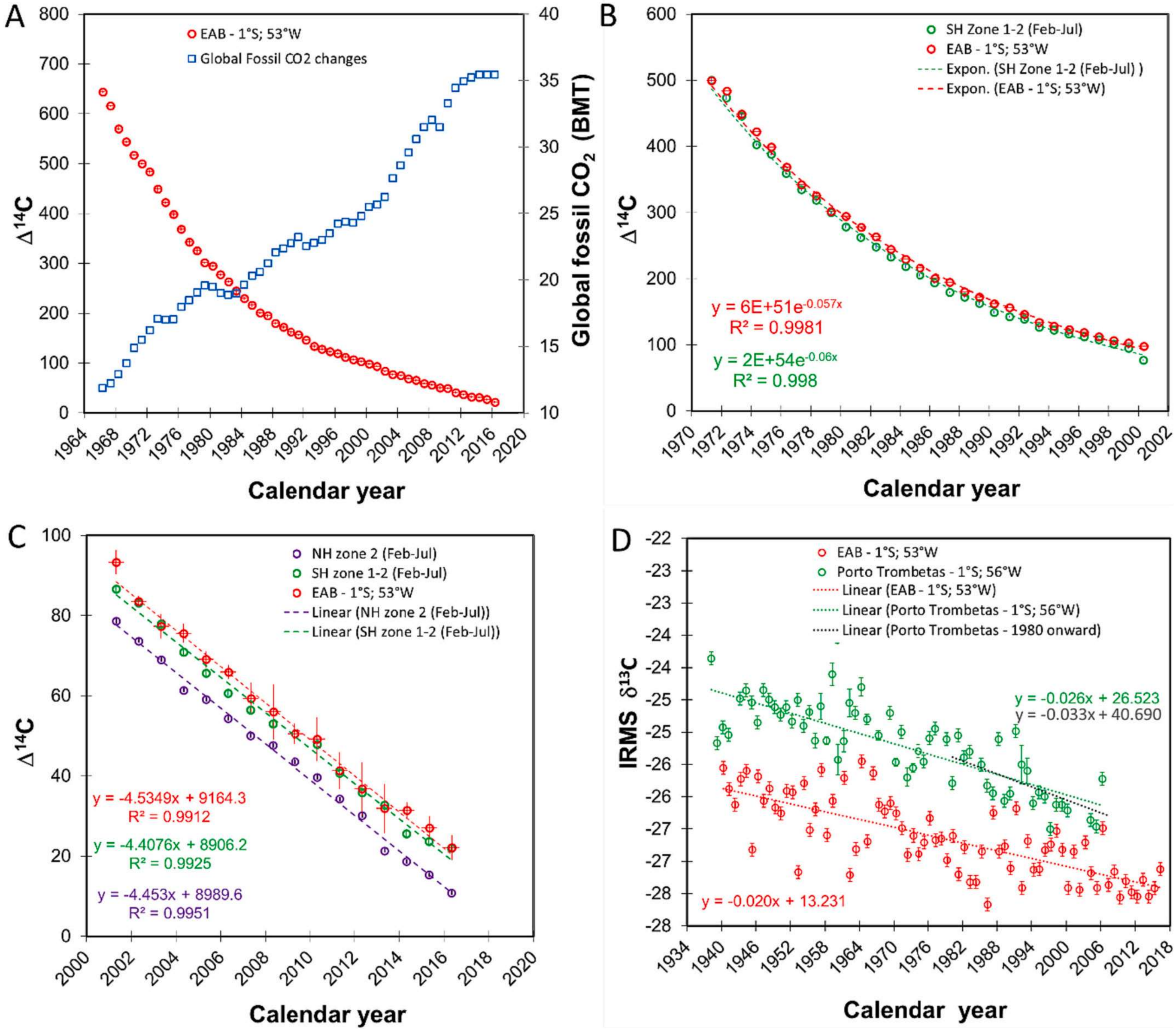

Fig. 8. Post-bomb maximum tree-ring EAB ^{14}C values (A) from 1966 to 2016 and the global fossil fuel atmospheric CO_2 trend in billion metric tons (BMT) for the same period estimated by Friedlingstein et al. (2023), (B) from 1971 to 2000 and the average atmospheric $\Delta^{14}C$ in February to July of each year based on the SH zone 1–2 compilation, (C) from 2001 to 2016, and the average atmospheric $\Delta^{14}C$ in February to July of each year based on both the NH zone 2 and SH zone 1–2 compilations, and (D) measured $\delta^{13}C$ in tree rings at two sites within the Amazon Basin are displayed, the EAB from 1940 to 2016 and Porto Trombetas from 1938 to 2007. Fitting results as exponential or linear are displayed on plots, as well as the coefficient of determination (R^2), when applicable.

network of robust, high-resolution ^{14}C datasets both within and in proximity to the TLPB. Such efforts will be crucial in advancing our knowledge in this area.

4. Conclusions

We have developed a detailed tree-ring ^{14}C record spanning from 1940 to 2016, encompassing 77 tree rings, from a moisture-sensitive tree-ring chronology located at the Equator's edge in the eastern Amazon Basin (1°S, 53°W). This record, comprising of 175 radiocarbon measurements, boasts high precision and accuracy, verified through replicated high-resolution ^{14}C measurements (deviation of <2.0 ‰; $n = 69$). Radiocarbon measurements were conducted using three different cellulose extraction procedures and further validated through inter-laboratory comparisons with UCI and ANSTO. Additionally, precise ^{14}C analysis of successive tree-ring cuts from the years 1962 and 1963, exhibiting rapid ^{14}C changes, provided insights into the radial growth patterns of this moisture-sensitive tree species.

We analyzed the complexity of ^{14}C concentrations over the Amazon Basin. Our approach involved comparing the ^{14}C record from the EAB with other pantropical tree-ring and atmospheric ^{14}C records. We employed the HYSPLIT backward trajectory analysis to trace the origins of air masses affecting two specific locations: the EAB in Brazil and Muna Island in Indonesia. This analysis covered two timeframes: stationary sources from the past 5 to 25 days (or −120 to −600 h) for the period 1949 to 2016, and a time-series snapshot at −600 h in the past. Additionally, we visualized the GP of air masses reaching the EAB site in the 1 to 5 days prior (−24 to −120 h), highlighting the influx of interhemispheric air during February to July, during the growth period of *C. odorata* trees. Our evaluation of the EAB ^{14}C data led to identifying specific correlations:

1) During the early bomb period from 1955 to 1960, we observed lower $\Delta^{14}C$ values in the EAB compared to the SH zone 3 compilation. This supports previous claims about a negative ^{14}C isoflux from the biosphere over land.
2) We also noted radiocarbon asymmetry between records at similar latitudes but separated by approximately 180° in longitude (EAB at 1°S, 53°W and Muna Island at 5°S, 122°E). Nonetheless, the EAB ^{14}C record aligns closely with the Central Equatorial Amazon, Porto Trombetas, Brazil (1°S, 56°W) record. This similarity suggests that the differences between EAB and SH zone 3 (i.e., Muna Island at 5°S, 122°E) are due to distinct cross-equatorial air mass transport from the NH extratropical surface along the TLPB region, as indicated by backward trajectory analysis.
3) The peak $\Delta^{14}C$ value at EAB was recorded as 674 ± 2 ‰ ($n = 2$) in April 1965. This peak value at EAB indicates that the inter-hemispheric time lag $\Delta^{14}C\text{-}CO_2$ transfer is close to 1 year.
4) We detected a $\Delta^{14}C$ enrichment in the EAB ^{14}C record, influenced by a positive biosphere reservoir effect on transferred Atlantic Ocean extratropical air masses, that began a decade earlier than models initially predicted and lasted for about three decades (1970 to 2000).
5) From the 2000s onward, the EAB ^{14}C record shows a drop, aligning with mid to high-latitude records in the SH. This shift in the EAB ^{14}C record marks the transition from the bomb to the fossil fuel era in the TLPB. While atmospheric fossil-fuel CO_2 emissions have been increasing steadily since the Industrial Revolution, the atmospheric $^{14}CO_2$ disequilibrium caused by aboveground nuclear bomb tests obscured the fossil CO_2 signal across mid- to high-latitudes in both hemispheres until the 1990s. A similar pattern was expected in the tropics within the same timeframe. However, our findings suggest that the positive biosphere effect over the Amazon Basin may have delayed these observations until the early 2000s.

Our newly established atmospheric ^{14}C record from the Equatorial Amazon Basin, based on absolutely dated tree rings and spanning the last 70 years, offers valuable insights into the historical variations of ^{14}C concentrations over the TLPB region. Although this record covers a relatively recent period, it is crucial for understanding past temporal and spatial variations in ^{14}C levels. Current climate models rely on accurate baseline data to identify key drivers of climate change. Therefore, our comprehensive ^{14}C record is expected to be highly beneficial for assessing ongoing and future changes affecting tropical regions. To gain a more complete understanding of historical and potentially recent shifts due to ongoing anthropogenic atmospheric disturbances, it is essential to expand ^{14}C observations in the TLPB region, particularly in areas like Africa, Indonesia, and the Pacific Islands.

CRediT authorship contribution statement

Guaciara M. Santos: Writing – original draft, Visualization, Validation, Supervision, Resources, Project administration, Methodology, Investigation, Funding acquisition, Formal analysis, Data curation, Conceptualization. **Daniela Granato-Souza:** Writing – review & editing, Visualization, Resources, Methodology, Formal analysis. **Santiago Ancapichún:** Writing – original draft, Visualization, Investigation, Formal analysis. **Rose Oelkers:** Writing – review & editing, Resources, Methodology. **Heather A. Haines:** Writing – review & editing, Validation, Resources, Methodology. **Ricardo De Pol-Holz:** Writing – review & editing, Validation. **Laia Andreu-Hayles:** Writing – review & editing, Resources, Methodology, Funding acquisition. **Quan Hua:** Writing – review & editing, Validation, Resources, Methodology. **Ana Carolina Barbosa:** Writing – review & editing, Visualization, Resources, Methodology, Investigation, Formal analysis.

Declaration of competing interest

The authors declare that they have no known competing financial interests or personal relationships that could have appeared to influence the work reported in this paper.

Data availability

Data will be made available on request (contact corresponding author) and later at IntCal dataset repository. Supporting information used for comparisons are properly cited in text and reference list.

Acknowledgements

This research was supported by the United States National Science Foundation (AGS-1903690 to G.M.S. and AGS-1903687 to L.A-H). S.A. was supported by PROYECTO CONICYT-BMBF 180005: AVOID. A.C.B. was supported by Conselho Nacional de Desenvolvimento Científico e Tecnológico (CNPq: PQ 313129/2022-3) and Fundação de Amparo à Pesquisa do Estado de Minas Gerais (Fapemig: APQ-01544-22). R.D.P acknowledges financial support from the Chilean ANID-FONDECYT 1201810 grant. G.M.S. thanks the valuable help of the undergrad students from UCI, Anita S. Yayi Komatsu, Jazmine M. Jr. Renteria for assistance on laboratory procedures, and Zhen Chen for assistance on sample isotope analysis. Q.H. acknowledges the financial support from the Australian Government through the National Collaborative Research Infrastructure Strategy for AMS radiocarbon analysis at the Centre for Accelerator Science at ANSTO.

Appendix A. Supplementary data

Supplementary data to this article can be found online at https://doi.org/10.1016/j.scitotenv.2024.170686.

References

Aldrian, E., Susanto, R.D., 2003. Identification of three dominant rainfall regions within Indonesia and their relationship to sea surface temperature. Int. J. Climatol. 23 (12), 1435–1452.

Ancapichún, S., De Pol-Holz, R., Christie, D.A., Santos, G.M., Collado-Fabbri, S., Garreaud, R., Lambert, F., Orfanoz-Cheuquelaf, A., Rojas, M., Southon, J., Turnbull, J.C., Creasman, P.P., 2021. Radiocarbon bomb-peak signal in tree-rings from the tropical Andes register low latitude atmospheric dynamics in the southern hemisphere. Sci. Total Environ. 774, 145126 https://doi.org/10.1016/j.scitotenv.2021.145126.

Ancapichún, S., Pawlyta, J., Rakowski, A.Z., Sieczkowska, D., 2022. Influence of air parcels from northern and southern hemispheres on radiocarbon-based Inca chronology. Radiocarbon 64 (6), 1431–1446. https://doi.org/10.1017/RDC.2022.87.

Andela, N., Morton, D.C., Schroeder, W., Chen, Y., Brando, P.M., Randerson, J.T., 2022. Tracking and classifying Amazon fire events in near real time. Sci. Adv. 8 (30), eabd2713.

Andreu-Hayles, L., Levesque, M., Martin-Benito, D., Huang, W., Harris, R., Oelkers, R., Leland, C., Martin-Fernández, J., Anchukaitis, K.J., Helle, G., 2019. A high yield cellulose extraction system for small whole wood samples and dual measurement of carbon and oxygen stable isotopes. Chem. Geol. 504, 53–65. https://doi.org/10.1016/j.chemgeo.2018.09.007.

Aramaki, T., Mizushima, T., Kuji, T., Povinec, P.P., Togawa, O., 2001. Distribution of radiocarbon in the southwestern North Pacific. Radiocarbon 43 (2B), 857–867.

Baker, J.C., Santos, G.M., Gloor, M., Brienen, R.J., 2017. Does Cedrela always form annual rings? Testing ring periodicity across South America using radiocarbon dating. Trees 31 (6), 1999–2009. https://doi.org/10.1007/s00468-017-1604-9.

Beverly, R.K., Beaumont, W., Tauz, D., Ormsby, K.M., von Reden, K.F., Santos, G.M., Southon, J.R., 2010. The Keck Carbon Cycle AMS Laboratory, University of California, Irvine: status report. Radiocarbon 52 (2), 301–309.

Blackaby, E., 2022. Variation in Soil Organic Carbon Across Lowland Tropical Forest Gradients: Soil Fertility and Precipitation Effects on Soil Carbon Organic Chemistry and Age (Doctoral dissertation). Colorado State University.

Borchert, R., Renner, S.S., Calle, Z., Navarrete, D., Tye, A., Gautier, L., Spichiger, R., von Hildebrand, P., 2005. Photoperiodic induction of synchronous flowering near the equator. Nature 433, 627–629.

Borchert, R., Calle, Z., Strahler, A.H., Baertschi, A., Magill, R.E., Broadhead, J.S., Kamau, J., Njoroge, J., Muthuri, C., 2015. Insolation and photoperiodic control of tree development near the equator. New Phytol. 205, 7–13.

Botía, S., Komiya, S., Marshall, J., Koch, T., Gałkowski, M., Lavric, J., Gomes-Alves, E., Walter, D., Fisch, G., Pinho, D.M., Nelson, B.W., 2022. The CO2 record at the Amazon Tall Tower Observatory: a new opportunity to study processes on seasonal and inter-annual scales. Glob. Chang. Biol. 28 (2), 588–611.

Brienen, R.J., Helle, G., Pons, T.L., Guyot, J.L., Gloor, M., 2012. Oxygen isotopes in tree rings are a good proxy for Amazon precipitation and El Niño-Southern Oscillation variability. Proc. Natl. Acad. Sci. 109 (42), 16957–16962.

Broecker, W.S., Gerard, R., Ewing, M., Heezen, B.C., 1960. Natural radiocarbon in the Atlantic Ocean. J. Geophys. Res. 65 (9), 2903–2931.

Bronk Ramsey, C., 2023. Radiocarbon calibration: from bane to blessing. Radiocarbon. https://doi.org/10.1017/RDC.2023.32.

Cain, W.F., Suess, H.E., 1976. Carbon 14 in tree rings. J. Geophys. Res. 81 (21), 3688–3694.

Carrasco, J.J., Neff, J.C., Harden, J.W., 2006. Modeling physical and biogeochemical controls over carbon accumulation in a boreal forest soil. J. Geophys. Res. Biogeo. 111 (G2).

Ciais, P., Tan, J., Wang, X., Roedenbeck, C., Chevallier, F., Piao, S.L., Moriarty, R., Broquet, G., Le Quéré, C., Canadell, J.G., Peng, S., 2019. Five decades of northern land carbon uptake revealed by the interhemispheric CO2 gradient. Nature 568 (7751), 221–225.

Dlugokencky, E., Trans, P., 2020. NOAA/GML, trends in atmospheric carbon dioxide. www.esrl.noaa.gov/gmd/ccgg/trends/.

Draxler, R., Taylor, D., 1982. Horizontal dispersion parameters for long-range transport modelling. J. Appl. Meteorol. 21 (3), 367–372. https://doi.org/10.1175/1520-0450(1982)021<0367:HDPFLR>2.0.CO;2.

Dutta, K., 2002. Coherence of tropospheric 14CO2 with El Niño/Southern Oscillation. Geophys. Res. Lett. 29 (20) (48-1).

Enting, I.G., 1982. Nuclear Weapons Data for Use in Carbon Cycle Modelling (No. 44). Commonwealth Scientific and Industrial Research Organization, Australia, pp. 1–19.

Fairhall, A.W., Young, A.W., 1985. Historical 14C measurements from the Atlantic, Pacific and Indian oceans. Radiocarbon 27 (3), 473–507.

Fan, S.M., Wofsy, S.C., Bakwin, P.S., Jacob, D.J., Fitzjarrald, D.R., 1990. Atmosphere-biosphere exchange of CO2 and O3 in the central Amazon forest. J. Geophys. Res. Atmos. 95 (D10), 16851–16864.

Fialho, W.M., Carvalho, L.M., Gan, M.A., Veiga, S.F., 2023. Mechanisms controlling persistent South Atlantic Convergence Zone events on intraseasonal timescales. Theor. Appl. Climatol. 152 (1–2), 75–96.

Fink, D., Hotchkis, M., Hua, Q., Jacobsen, G., Smith, A.M., Zoppi, U., Child, D., Mifsud, C., van der Gaast, H., Williams, A., Williams, M., 2004. The ANTARES AMS Facility at ANSTO. Nucl. Instrum. Methods Phys. Res. B 223–224, 109–115.

Friedlingstein, P., O'sullivan, M., Jones, M.W., Andrew, R.M., Gregor, L., Hauck, J., Le Quéré, C., Luijkx, I.T., Olsen, A., Peters, G.P., Peters, W., 2022. Global carbon budget 2022. Earth Syst. Sci. Data Discuss. 2022, 1–159.

Friedlingstein, P., O'sullivan, M., Jones, M.W., Andrew, R.M., Bakker, D.C., Hauck, J., Landschützer, P., Le Quéré, C., Luijkx, I.T., Peters, G.P., Peters, W., 2023. Global carbon budget 2023. Earth Syst. Sci. Data 15 (12), 5301–5369.

Gallego, D., García-Herrera, R., Losada, T., Mohino, E., Rodríguez de Fonseca, B., 2021. A shift in the wind regime of the southern end of the canary upwelling system at the turn of the 20th century. J. Geophys. Res. Oceans 126 (5) (p.e2020JC017093).

Garreaud, R.D., Vuille, M., Compagnucci, R., Marengo, J., 2009. Present day South American climate. Palaeogeogr. Palaeoclimatol. Palaeoecol. 281, 180–195.

Granato-Souza, D., Stahle, D.W., Barbosa, A.C., Feng, S., Torbenson, M.C., de Assis Pereira, G., Schöngart, J., Barbosa, J.P., Griffin, D., 2019. Tree rings and rainfall in the equatorial Amazon. Climate Dynam. 52 (3), 1857–1869. https://doi.org/10.1007/s00382-018-4227-y.

Granato-Souza, D., Stahle, D.W., Torbenson, M.C., Howard, I.M., Barbosa, A.C., Feng, S., Fernandes, K., Schöngart, J., 2020. Multidecadal changes in wet season precipitation totals over the Eastern Amazon. Geophys. Res. Lett. 47 (8) (p.e2020GL087478).

Graven, H.D., Guilderson, T.P., Keeling, R.F., 2012. Observations of radiocarbon in CO2 at seven global sampling sites in the Scripps flask network: analysis of spatial gradients and seasonal cycles. J. Geophys. Res. Atmos. 117 (D02303) https://doi.org/10.1029/2011JD016535.

Graven, H., Allison, C.E., Etheridge, D.M., Hammer, S., Keeling, R.F., Levin, I., Meijer, H. A., Rubino, M., Tans, P.P., Trudinger, C.M., Vaughn, B.H., 2017. Compiled records of carbon isotopes in atmospheric CO2 for historical simulations in CMIP6. Geosci. Model Dev. 10 (12), 4405–4417.

Grootes, P.M., Farwell, G.W., Schmidt, F.H., Leach, D.D., Stuiver, M., 1989. Rapid response of tree cellulose radiocarbon content to changes in atmospheric 14CO2 concentration. Tellus B 41 (2), 134–148.

Harrison, K.G., 1996. Using bulk soil radiocarbon measurements to estimate soil organic matter turnover times: implications for atmospheric CO2 levels. Radiocarbon 38 (2), 181–190.

Hogg, A., Heaton, T.J., Hua, Q., Palmer, J.G., Turney, C.S.M., Southon, J., Bayliss, A., Blackwell, P.G., Boswijk, G., Bronk Ramsey, C., Pearson, C., Petchey, F., Reimer, P., Reimer, R., Wacker, L., 2020. SHCal20 southern hemisphere calibration, 0-55,000 years cal BP. Radiocarbon 62 (4), 759–778. https://doi.org/10.1017/RDC.2020.59.

Houghton, R.A., Castanho, A., 2023. Annual emissions of carbon from land use, land-use change, and forestry from 1850 to 2020. Earth Syst. Sci. Data 15 (5), 2025–2054.

Hua, Q., Barbetti, M., Jacobsen, G.E., Zoppi, U., Lawson, E.M., 2000. Bomb radiocarbon in annual tree rings from Thailand and Tasmania. Nucl. Inst. Methods Phys. Res. B 172 (1–4), 359–365.

Hua, Q., Jacobsen, G.E., Zoppi, U., Lawson, E.M., Williams, A.A., Smith, A.M., McGann, M.J., 2001. Progress in radiocarbon target preparation at the ANTARES AMS Centre. Radiocarbon 43, 275–282.

Hua, Q., Barbetti, M., Zoppi, U., Chapman, D.M., Thomson, B., 2003. Bomb radiocarbon in tree rings from northern New South Wales, Australia: implications for dendrochronology, atmospheric transport and air-sea exchange of CO_2. Radiocarbon 45 (3), 431–447.

Hua, Q., Barbetti, M., Zoppi, U., Fink, D., Watanasak, M., Jacobsen, G.E., 2004. Radiocarbon in tropical tree rings during the Little Ice Age. Nucl. Instrum. Methods Phys. Res. B 223-224, 489–494.

Hua, Q., Barbetti, M., Levchenko, V.A., D'Arrigo, R.D., Buckley, B.M., Smith, A.M., 2012. Monsoonal influences on Southern Hemisphere $^{14}CO_2$. Geophys. Res. Lett. 39, L19806. https://doi.org/10.1029/2012GL052971.

Hua, Q., Turnbull, J.C., Santos, G.M., Rakowski, A.Z., Ancapichún, S., De Pol-Holz, R., Hammer, S., Lehman, S.J., Levin, I., Miller, J.B., Palmer, J.G., 2022. Atmospheric radiocarbon for the period 1950–2019. Radiocarbon 64 (4), 723–745. https://doi.org/10.1017/RDC.2021.95.

Kalnay, E., Kanamitsu, M., Kistler, R., Collins, W., Deaven, D., Gandin, L., et al., 1996. The NCEP/NCAR 40-year reanalysis project. Bull. Am. Meteorol. Soc. 77, 437–471. https://doi.org/10.1175/1520-0477(1996)077<0437:TNYRP>2.0.CO;2.

Keeling, R.F., Graven, H.D., Welp, L.R., Resplandy, L., Bi, J., Piper, S.C., Sun, Y., Bollenbacher, A., Meijer, H.A., 2017. Atmospheric evidence for a global secular increase in carbon isotopic discrimination of land photosynthesis. Proc. Natl. Acad. Sci. 114 (39), 10361–10366.

Kutschera, W., 2022. The versatile uses of the 14C bomb peak. Radiocarbon 1–14.

Lawrence, C.R., Beem-Miller, J., Hoyt, A.M., Monroe, G., Sierra, C.A., Stoner, S., 2020. An open-source database for the synthesis of soil radiocarbon data: International Soil Radiocarbon Database (ISRaD) version 1.0. Earth Syst. Sci. Data 12, 61–76. https://doi.org/10.5194/essd-12-61-2020.

Levin, I., Hesshaimer, V., 2000. Radiocarbon–a unique tracer of global carbon cycle dynamics. Radiocarbon 42, 69–80.

Levin, I., Kromer, B., Francey, R.J., 1996. Continuous measurements of ^{14}C in atmospheric CO_2 at Cape Grim. In: Francey, R.J., Dick, A.L., Derek, N. (Eds.), Baseline Atmospheric Program Australia 1994–1995. CSIRO, Melbourne, pp. 106–107.

Levin, I., Kromer, B., Francey, R.J., 1999. Continuous measurements of ^{14}C in atmospheric CO_2 at Cape Grim, 1995–1996. In: Grass, J.L., Derek, N., Tindale, N.W., Dick, A.L. (Eds.), Baseline Atmospheric Program Australia 1996. Bureau of Meteorology and CSIRO Atmospheric Research, Melbourne, pp. 89–90.

Levin, I., Naegler, T., Kromer, B., Diehl, M., Francey, R.J., Gomez-Pelaez, A.J., Steele, L. P., Wagenbach, D., Weller, R., Worthy, D.E., 2010. Observations and modelling of the global distribution and long-term trend of atmospheric 14CO2. Tellus B 62B, 26–46.

Levin, I., Kromer, B., Steele, L.P., Porter, L.W., 2011. Continuous measurements of ^{14}C in atmospheric CO_2 at cape grim, 1997-2008. In: Derek, N., Krummel, P.B. (Eds.), Baseline Atmospheric Program Australia 2007–2008. Australian Bureau of Meteorology and CSIRO Marine and Atmospheric Research, Melbourne, pp. 56–59.

Levin, I., Hammer, S., Kromer, B., Preunkert, S., Weller, R., Worthy, D.E., 2022. Radiocarbon in global tropospheric carbon dioxide. Radiocarbon 64 (4), 781–791.

Manning, M.R., Lowe, D.C., Melhuish, W.H., Sparks, R.J., Wallace, G., Brenninkmeijer, C.A.M., McGrill, R.C., 1990. The use of radiocarbon measurements in atmospheric studies. Radiocarbon 32 (1), 37–58.

Meijer, H.A.J., Pertuisot, M.H., van der Plicht, J., 2006. High accuracy ^{14}C measurements for atmospheric CO_2 samples by AMS. Radiocarbon 48 (3), 355–372.

Morgan, W.T., Darbyshire, E., Spracklen, D.V., Artaxo, P., Coe, H., 2019. Non-deforestation drivers of fires are increasingly important sources of aerosol and carbon dioxide emissions across Amazonia. Sci. Rep. 9 (1), 1–15.

Naegler, T., Levin, I., 2009. Biosphere-atmosphere gross carbon exchange flux and the δ13CO2 and Δ14CO2 disequilibria constrained by the biospheric excess radiocarbon inventory. J. Geophys. Res. 114, D17303. https://doi.org/10.1029/2008JD011116.

Ndeye, M., 2008. Marine reservoir ages in northern Senegal and Mauritania coastal waters. Radiocarbon 50 (2), 281–288.

Nydal, R., Lövseth, K., 1996. Carbon-14 Measurement in Atmospheric CO_2 from Northern and Southern Hemisphere Sites, 1962–1993. Carbon Dioxide Information Analysis Center, World Data Center-A for Atmospheric Trace Gases, Oak Ridge National Laboratory, Tennessee.

Nydal, R., Brenkert, A.L., Boden, T.A. (Eds.), 1998. Carbon-14 Measurements in Surface Water CO2 from the Atlantic, Indian and Pacific Oceans, 1965-1994. Carbon Dioxide Information Analysis Center, Oak Ridgey National Laboratory, Oak Ridge, TN, p. 131. https://doi.org/10.3334/CDIAC/otg.ndp057. ORNL/CDIAC-104, NDP-057A.

Park, J.H., Kim, J.C., Cheoun, M.K., Kim, I.C., Youn, M., Liu, Y.H., Kim, E.S., 2002. 14C level at Mt Chiak and Mt Kyeryong in Korea. Radiocarbon 44 (2), 559–566.

Randel, W.J., Park, M., 2006. Deep convective influence on the Asian summer monsoon anticyclone and associated tracer variability observed with Atmospheric Infrared Sounder (AIRS). J. Geophys. Res. Atmos. 111 (D12).

Randerson, J.T., Enting, I.G., Schuur, E.A.G., Caldeira, K., Fung, I.Y., 2002. Seasonal and latitudinal variability of troposphere Δ14CO2: post bomb contributions from fossil fuels, oceans, the stratosphere, and the terrestrial biosphere. Global Biogeochem. Cycles 16 (4) (59-1).

Reimer, P.J., Austin, W.E., Bard, E., Bayliss, A., Blackwell, P.G., Bronk Ramsey, C., Butzin, M., Cheng, H., Edwards, R.L., Friedrich, M., Grootes, P.M., 2020. The IntCal20 Northern Hemisphere radiocarbon age calibration curve (0–55 cal kBP). Radiocarbon 62 (4), 725–757. https://doi.org/10.1017/RDC.2020.41.

Rozanski, K., Stichler, W., Gonfiantini, R., Scott, E.M., Beukens, R.P., Kromer, B. van der, Plicht, J., 1992. The IAEA 14C Intercomparison exercise 1990. Radiocarbon 34, 506–519.

Santos, G.M., Xu, X., 2017. Bag of tricks: a set of techniques and other resources to help 14C laboratory setup, sample processing, and beyond. Radiocarbon 59 (3), 785–801.

Santos, G.M., Moore, R., Southon, J., Griffin, S., Hinger, E., Zhang, D., 2007. AMS 14C preparation at the KCCAMS/UCI Facility: status report and performance of small samples. Radiocarbon 49 (2), 255–269.

Santos, G.M., Linares, R., Lisi, C.S., Tomazello Filho, M., 2015. Annual growth rings in a sample of Paraná pine (Araucaria angustifolia): toward improving the 14C calibration curve for the Southern Hemisphere. Quaternary Geochronol. 25, 96–103.

Santos, G.M., Granato-Souza, D., Barbosa, A.C., Oelkers, R., Andreu-Hayles, L., 2020. Radiocarbon analysis confirms annual periodicity in Cedrela odorata tree rings from the equatorial Amazon. Quat. Geochronol. 58, 101079 https://doi.org/10.1016/j.quageo.2020.101079.

Santos, G.M., Albuquerque, R.P., Barros, C.F., Ancapichún, S., Oelkers, R., Andreu-Hayles, L., De Faria, S.M., De Pol-Holz, R., das Neves Brandes, A.F., 2022. High-precision 14C measurements of parenchyma-rich Hymenolobium petraeum tree species confirm bomb-peak atmospheric levels and reveal local fossil-fuel CO2 emissions in the Central Amazon. Environ. Res. 214, 113994.

Santos, G.M., Komatsu, A.S., Renteria Jr., J.M., Brandes, A.F., Leong, C.A., Collado-Fabbri, S., De Pol-Holz, R., 2023. A universal approach to alpha-cellulose extraction for radiocarbon analysis of 14C-free to post-bomb ages. Quaternary Geochronol. 74, 101414.

Scott, M., Cook, G., Harkness, D., Naysmith, Bryant, C., 2003a. The fourth international radiocarbon comparison (FIRI) – sections 1-10. Radiocarbon 45, 135–290.

Scott, M., Cook, G., Harkness, D., Naysmith, P., 2003b. Part 2: the third international radiocarbon comparison (TIRI). Radiocarbon 45, 293–328.

Shi, Z., Allison, S.D., He, Y., Levine, P.A., Hoyt, A.M., Beem-Miller, J., Zhu, Q., Wieder, W.R., Trumbore, S., Randerson, J.T., 2020. The age distribution of global soil carbon inferred from radiocarbon measurements. Nat. Geosci. 13 (8), 555–559.

Stahle, D.W., Torbenson, M.C.A., Howard, I.M., Granato-Souza, D., Barbosa, A.C., Feng, S., Schöngart, J., López, L., Villalba, R., Villanueva, J., Fernandes, K., 2020. Pan American interactions of Amazon precipitation, streamflow, and tree growth extremes. Environ. Res. Lett. 15 (10), 104092.

Stein, A., Draxler, R., Rolph, G., Stunder, B., Cohen, M., Ngan, F., 2015. NOAA's HYSPLIT atmospheric transport and dispersion modeling system. Bull. Am. Meteorol. Soc. 96, 2059–2077. https://doi.org/10.1175/BAMS-D-14-00110.1.

Stuiver, M., Polach, H.A., 1977. Discussion: reporting of 14C data. Radiocarbon 19 (3), 355–363.

Suess, H.E., 1955. Radiocarbon concentration in modern wood. Science 122 (3166), 415–417.

Svarva, H., Grootes, P., Seiler, M., Stene, S., Thun, T., Værnes, E., Nadeau, M.J., 2019. The 1953–1965 rise in atmospheric bomb 14C in central Norway. Radiocarbon 61 (6), 1765–1774.

Tans, P.P., De Jong, A.F.M., Mook, W.G., 1978. Chemical pretreatment and radial flow of 14C in tree rings. Nature 271 (5642), 234–235.

Thampi, B.V., Rajeev, K., Parameswaran, K., Mishra, M.K., 2009. Spatial distribution of the Southeast Asian smoke plume over the Indian Ocean and its radiative heating in the atmosphere during the major fire event of 2006. Geophys. Res. Lett. 36 (16).

Toggweiler, J.R., Druffel, E.R., Key, R.M., Galbraith, E.D., 2019. Upwelling in the ocean basins north of the ACC: 1. On the upwelling exposed by the surface distribution of Δ14C. J. Geophys. Res. Oceans 124 (4), 2591–2608.

Trumbore, S.E., Zheng, S., 1996. Comparison of fractionation methods for soil organic matter 14C analysis. Radiocarbon 38 (2), 219–229.

Turnbull, J.C., Mikaloff Fletcher, S.E., Brailsford, G.W., Moss, R.C., Norris, M.W., Steinkamp, K., 2017. Sixty years of radiocarbon dioxide measurements at Wellington, New Zealand: 1954–2014. Atmos. Chem. Phys. 17 (23), 14771–14784.

Turney, C.S., Palmer, J.G., 2007. Does the El Niño–Southern Oscillation control the interhemispheric radiocarbon offset? Quatern. Res. 67 (1), 174–180.

Turney, C.S.M., Palmer, J., Maslin, M.A., et al., 2018. Global peak in atmospheric radiocarbon provides a potential definition for the onset of the anthropocene epoch in 1965. Sci. Rep. 8, 3293. https://doi.org/10.1038/s41598-018-20970-5.

Vogel, J.C., Marais, M., 1971. Pretoria radiocarbon dates I. Radiocarbon 13 (2), 378–394.

Wagner, A.J., Guilderson, T.P., Slowey, N.C., Cole, J.E., 2009. Pre-bomb surface water radiocarbon of the Gulf of Mexico and Caribbean as recorded in hermatypic corals. Radiocarbon 51 (3), 947–954.

Waugh, D.W., Crotwell, A.M., Dlugokencky, E.J., Dutton, G.S., Elkins, J.W., Hall, B.D., Hintsa, E.J., Hurst, D.F., Montzka, S.A., Mondeel, D.J., Moore, F.L., 2013. Tropospheric SF6: Age of air from the Northern Hemisphere midlatitude surface. J. Geophys. Res. Atmos. 118 (19), 411–429. https://doi.org/10.1002/jgrd.50848.

Westbrook, J.A., Guilderson, T.P., Colinvaux, P.A., 2006. Annual growth rings in a sample of Hymenaea courbaril. IAWA J. 27 (2), 193–197.

Wiggins, E.B., Czimczik, C.I., Santos, G.M., Chen, Y., Xu, X., Holden, S.R., Randerson, J.T., Harvey, C.F., Kai, F.M., Yu, L.E., 2018. Smoke radiocarbon measurements from Indonesian fires provide evidence for burning of millennia-aged peat. Proc. Natl. Acad. Sci. 115 (49), 12419–12424.

Wu, X., Yang, H., Waugh, D.W., Orbe, C., Tilmes, S., Lamarque, J.F., 2018. Spatial and temporal variability of interhemispheric transport times. Atmos. Chem. Phys. 18 (10), 7439–7452.

Xiong, X., Zhou, W., Hou, X., Cheng, P., Du, H., Zhao, X., Wu, S., Hou, Y., Lu, X., Fu, Y., 2021. Time series of atmospheric Δ14CO2 recorded in tree rings from Northwest China (1957–2015). Chemosphere 272, 129921.

Yan, X., Konopka, P., Ploeger, F., Podglajen, A., Wright, J.S., Müller, R., Riese, M., 2019. The efficiency of transport into the stratosphere via the Asian and North American summer monsoon circulations. Atmos. Chem. Phys. 19 (24), 15629–15649.

Yan, X., Konopka, P., Hauck, M., Podglajen, A., Ploeger, F., 2021. Asymmetry and pathways of inter-hemispheric transport in the upper troposphere and lower stratosphere. Atmos. Chem. Phys. 21 (9), 6627–6645.

Zilli, M.T., Carvalho, L.M., Lintner, B.R., 2019. The poleward shift of South Atlantic Convergence Zone in recent decades. Climate Dynam. 52, 2545–2563.